REPORT DOCUMENTATION PAGE

AFRL-SR-BL-TR-01-

0081

1. AGENCY USE ONLY *(Leave blank)*	2. REPORT DATE	3. REPORT TYPE AND DATES COVERED
	FINAL	15 NOVEMBER 1998 TO 30 SEPTEMBER 2000

4. TITLE AND SUBTITLE
Parallel Multigrid DNS/LES Methods for Time-Dependent Compressible Turbulent Flow Around 3-D Airfoils

5. FUNDING NUMBERS
F49620-99-1-0042

6. AUTHOR(S)
Chaoguin Liu, Hua Shan, Li Jiang

7. PERFORMING ORGANIZATION NAME(S) AND ADDRESS(ES)
Center for Numerical Simulation and Modeling
College of Engineering and Science
Louisana Tech University
P.O.Box 10348
Ruston, Louisiana, 71272

8. PERFORMING ORGANIZATION REPORT NUMBER

9. SPONSORING/MONITORING AGENCY NAME(S) AND ADDRESS(ES)
AFOSR/NM
801 North Randolph Street Room,732
Arlington, VA 22203-1977

10. SPONSORING/MONITORING AGENCY REPORT NUMBER
F49620-99-1-0042

11. SUPPLEMENTARY NOTES

12a. DISTRIBUTION AVAILABILITY STATEMENT
Unlimited Distribution

12b. DISTRIBUTION CODE

13. ABSTRACT *(Maximum 200 words)*

Direct numerical simulation has been carried out to simulate the flow around a slender fiat-plate delta wing at 12.5° angle of attack. Two Reynolds number have been selected. At a lower Reynolds number of 5 × 104, the flow is stable and dominated by a pair of leading-edge primary vortices. At a higher Reynolds number of 1.96 × 105, small-scale votical structures are shedding from the leading-edge. It has been found that the shedding of the small-scale vortical structures originates not only from the Kelvin-Helmhotz type instability of the leading-edge shear layer, but also from the separation of the secondary vortex form the wing surface. The interaction between the sec-ondary vortex and the Kelvin-Hehnholtz type vortex is of particular interesting. The periods of vortex shedding are obtained from the time series of velocity components. The distributions of the temporal-averaged velocity near the upper surface of the delta wing obtained from the com-putational results agree well with those from the experiment of Rieley ~ Lowson (1998). But the steady small-scale vortical structures observed in the same experiment have not been found in the current simulation results. However: some unsteady vortical structures were also observed in the experiment, which could be related to the unsteady small vortices found in the computational results.

14. SUBJECT TERMS			15. NUMBER OF PAGES 51
			16. PRICE CODE
17. SECURITY CLASSIFICATION OF REPORT	18. SECURITY CLASSIFICATION OF THIS PAGE	19. SECURITY CLASSIFICATION OF ABSTRACT	20. LIMITATION OF ABSTRACT

20010221 137

Parallel Multigrid DNS/LES Methods for Time-Dependent Compressible Turbulent Flow Around 3-D Airfoils *

Chaoqun Liu[†], Hua Shan[‡], Li Jiang[§]

Center for Numerical Simulation and Modeling
College of Engineering and Science
Louisiana Tech University
P.O. Box 10348
Ruston, Louisiana, U.S.A.

*This work is sponsored under AFOSR Grant F49620-99-1-0042 managed by Dr. L. Sakell
[†]Professor of Mathematics
[‡]Post-doctoral Research Associate
[§]Post-doctoral Research Associate

Chapter 1

Grid Generation for DNS/LES

1.1 Two-Dimensional Grid Generation

An elliptic grid generation method first proposed by Spekreuse (1995) is used to generate 2D grids. The elliptic grid generation method is based on a composite mapping, which is consisted of a nonlinear transfinite algebraic transformation and an elliptic transformation. The algebraic transformation maps the computational space $\mathcal{C}$ onto a parameter space $\mathcal{P}$, and the elliptic transformation maps the parameter space on to the physical domain $\mathcal{D}$. The computational space, parameter space, and the physical domain are illustrated in Figure 1.1.

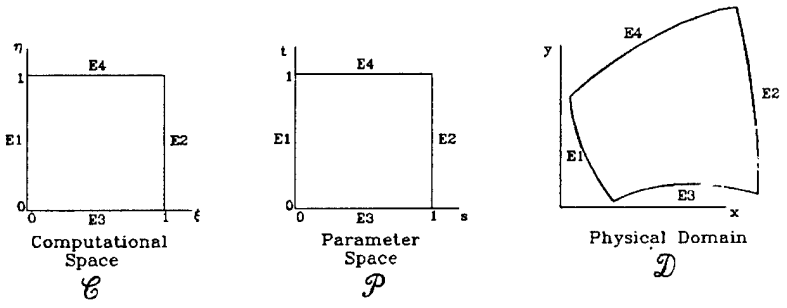

Figure 1.1: Computational space C, Parameter space P, and Physical domain D

The computational space $\mathcal{C}$ is defined as the unit square in a two-dimensional space with Cartesian coordinates (ξ, η), and $\xi \in [0,1]$, $\eta \in [0,1]$ (see Figure 1.1). The grids are uniformly distributed on the boundaries and in the interior area of the computational space. The mesh sizes are $\frac{1}{N_\xi - 1}$ in the ξ direction and $\frac{1}{N_\eta - 1}$ in the η direction, where N_ξ and N_η are the grid numbers in the corresponding direction. The parameter space $\mathcal{P}$ is defined as a unit space in a two-dimensional space with Cartesian coordinate (s,t), and $s \in [0,1]$, $t \in [0,1]$. The boundary values of s and t are determined by the grid point distribution in the physical domain.

- $s = 0$ at edge E_1 and $s = 1$ at edge E_2
- s is the normalized arc-length along edges E_3 and E_4

- $t = 0$ at edge E_3 and $t = 1$ at edge E_4
- t is the normalized arc-length along edges E_1 and E_2

An algebraic transformation $s : \mathcal{C} \to \mathcal{P}$ is defined to map the computational space $\mathcal{C}$ onto the parameter space $\mathcal{P}$. The grid distribution is specified by this algebraic transformation, which depends on the prescribed boundary grid point distribution. The interior grid point distribution inside the domain, generated by the algebraic transformation, is a good reflection of the prescribed boundary grid point distribution. Let $s_{E_3}(\xi) = s(\xi, 0)$ and $s_{E_4}(\xi) = s(\xi, 1)$ denote the normalized arc-length along edges E_3 and E_4, $t_{E_1}(\eta) = t(0, \eta)$ and $t_{E_2}(\eta) = t(1, \eta)$ denote the normalized arc-length along edges E_1 and E_2. The algebraic transformation $s : \mathcal{C} \to \mathcal{P}$ is defined as

$$\begin{aligned} s &= s_{E_3}(\xi)(1-t) + s_{E_4}(\xi)t \\ t &= t_{E_1}(\eta)(1-s) + t_{E_2}(\eta)s \end{aligned} \tag{1.1}$$

Equation (1.1) is called the algebraic straight line transformation. It defines a differentiable one-to-one mapping because of the positiveness of the Jacobian: $s_\xi t_\eta - s_\eta t_\xi > 0$.

The elliptic transformation $x : \mathcal{P} \to \mathcal{D}$, which is independent of the prescribed boundary grid point distribution, is defined to map the parameter space $\mathcal{P}$ onto the physical domain $\mathcal{D}$. The elliptic transformation is equivalent to a set of Laplace equations

$$\begin{aligned} s_{xx} + s_{yy} &= 0 \\ t_{xx} + t_{yy} &= 0 \end{aligned} \tag{1.2}$$

The elliptic transformation defined by the above equations is also differentiable and one-to-one.

Till now we have defined two transformations, i.e., the algebraic transformation $s : \mathcal{C} \to \mathcal{P}$, and the elliptic transformation $x : \mathcal{P} \to \mathcal{D}$. Because both the algebraic transformation and the elliptic transformation are differentiable and one-to-one. The composition the two transformation is also differentiable and one-to-one, so as to the inverse transformation.

In physical domain, the curvilinear coordinate system satisfies a system of Laplace equations:

$$\Delta \boldsymbol{r} = 0 \tag{1.3}$$

where $\boldsymbol{r} = (x, y)^T$. The inherent smoothness of the Laplace operator makes the grids smoothly distributed in the physical domain. Being transformed to the computational space, this Laplace system becomes a set of Poisson equations. The control functions is determined by the composed transformation according to the following procedures.

First, Eq.(1.2) is transformed into the computational space $\mathcal{C}$:

$$\begin{aligned} \Delta s &= g^{11}s_{\xi\xi} + 2g^{12}s_{\xi\eta} + g^{22}s_{\eta\eta} + \Delta\xi s_\xi + \Delta\eta s_\eta \\ \Delta t &= g^{11}t_{\xi\xi} + 2g^{12}t_{\xi\eta} + g^{22}t_{\eta\eta} + \Delta\xi t_\xi + \Delta\eta t_\eta \end{aligned} \tag{1.4}$$

where g^{11}, g^{12}, g^{22} are the components of the contravariant metric tensor, which can be calculated from the covariant metric tensor

$$\begin{aligned} g^{11} &= \frac{1}{J^2} g_{22} = (\boldsymbol{r}_\eta, \boldsymbol{r}_\eta)/J^2 \\ g^{12} &= -\frac{1}{J^2} g_{12} = -(\boldsymbol{r}_\xi, \boldsymbol{r}_\eta)/J^2 \\ g^{22} &= \frac{1}{J^2} g_{11} = (\boldsymbol{r}_\xi, \boldsymbol{r}_\xi)/J^2 \end{aligned}$$

J is defined as $\sqrt{det|g_{ij}|}$. From Eq.(1.2) and (1.4), we have

$$\begin{pmatrix} \Delta\xi \\ \Delta\eta \end{pmatrix} = g^{11}\mathbf{P}_{11} + 2g^{12}\mathbf{P}_{12} + g^{22}\mathbf{P}_{22} \tag{1.5}$$

where

$$\begin{aligned} \mathbf{P}_{11} &= \begin{pmatrix} P_{11}^{(1)} \\ P_{11}^{(2)} \end{pmatrix} = -\mathbf{T}^{-1} \begin{pmatrix} s_{\xi\xi} \\ t_{\xi\xi} \end{pmatrix} \\ \mathbf{P}_{12} &= \begin{pmatrix} P_{12}^{(1)} \\ P_{12}^{(2)} \end{pmatrix} = -\mathbf{T}^{-1} \begin{pmatrix} s_{\xi\eta} \\ t_{\xi\eta} \end{pmatrix} \\ \mathbf{P}_{22} &= \begin{pmatrix} P_{22}^{(1)} \\ P_{22}^{(2)} \end{pmatrix} = -\mathbf{T}^{-1} \begin{pmatrix} s_{\eta\eta} \\ t_{\eta\eta} \end{pmatrix} \end{aligned} \tag{1.6}$$

and the matrix $\mathbf{T}$ is defined as

$$\mathbf{T} = \begin{pmatrix} s_\xi & s_\eta \\ t_\xi & t_\eta \end{pmatrix} \tag{1.7}$$

Then the Laplace system Eq.(1.3) is transformed to the computational space C:

$$g^{11}\boldsymbol{r}_{\xi\xi} + 2g^{12}\boldsymbol{r}_{\xi\eta} + g^{22}\boldsymbol{r}_{\eta\eta} + \Delta\xi\boldsymbol{r}_\xi + \Delta\eta\boldsymbol{r}_\eta = 0 \tag{1.8}$$

Substitute Eq.(1.5) into Eq.(1.8), $\Delta\xi$ and $\Delta\eta$ are replaced by the control functions on the right-hand-side of Eq.(1.5), and we obtain the Poisson equations for the grid generation as follows:

$$g^{11}\boldsymbol{r}_{\xi\xi} + 2g^{12}\boldsymbol{r}_{\xi\eta} + g^{22}\boldsymbol{r}_{\eta\eta} + (g^{11}P_{11}^{(1)} + 2g^{12}P_{12}^{(1)} + g^{22}P_{22}^{(1)})\boldsymbol{r}_\xi + (g^{11}P_{11}^{(2)} + 2g^{12}P_{12}^{(2)} + g^{22}P_{22}^{(2)})\boldsymbol{r}_\eta = 0 \tag{1.9}$$

where the control functions $P_{11}^{(1)}, P_{12}^{(1)}, P_{22}^{(1)}, P_{11}^{(2)}, P_{12}^{(2)}, P_{22}^{(2)}$ are determined by the algebraic transformation, as defined previously in Eq.(1.6).

The elliptic transformation is carried by solving a set of Poisson equations. The control functions are specified by the algebraic transformation only and it is, therefore, not needed to compute the control functions at the boundary and to interpolate them into the interior of the domain, as required in the case for all well-known elliptic grid generation systems based on Poisson systems.

The computed grids are in general not orthogonal at the boundary. The algebraic transformation can be redefined to obtain a grid which is orthogonal at the boundary. First, redefine the elliptic transformation by imposing the following boundary conditions for s and t:

- $s = 0$ at edge E_1 and $s = 1$ at edge E_2
- $\frac{\partial s}{\partial n} = 0$ along edges E_3 and E_4, where n is the outward normal direction
- $t = 0$ at edge E_3 and $t = 1$ at edge E_4
- $\frac{\partial t}{\partial n} = 0$ along edges E_1 and E_2, where n is the outward normal direction

Second, redefine the algebraic transformation $s : \mathcal{C} \to \mathcal{P}$ according to two algebraic equations,

$$\begin{aligned} s &= s_{E_3}(\xi)H_0(t) + s_{E_4}(\xi)H_1(t) \\ t &= t_{E_1}(\eta)H_0(s) + t_{E_2}(\eta)H_1(s) \end{aligned} \tag{1.10}$$

where H_0 and H_1 are cubic Hermite interpolation functions defined as

$$\begin{aligned} H_0(s) &= (1+2s)(1-s)^2 \\ H_1(s) &= (3-2s)s^2 \end{aligned} \tag{1.11}$$

Grid orthogonality at boundaries is obtained in three steps.

1. Compute an initial grid based on the Poission grid generation system with control functions specified according to the algebraic straight line transformation defined by Eq.1.1;
2. Solve the two Laplace equations given by Eq.1.2 with the above specified boundary conditions;
3. Recompute the grid based on the Poisson system but with control functions specified according to the algebraic transformation defined by Eq.1.10.

The two-dimensional grid near the leading edge of a Joukowsky airfoil is shown in Figure 1.2.

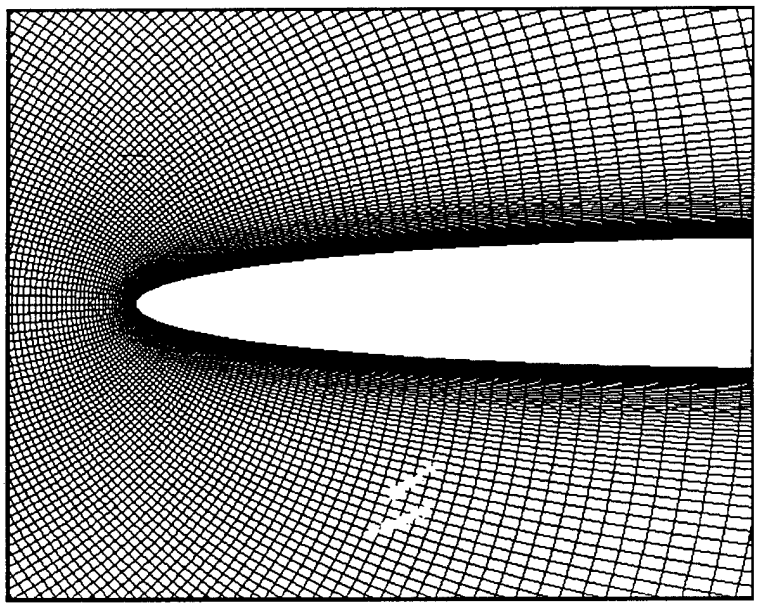

Figure 1.2: Grid near the leading edge of a Joukowsky airfoil

1.2 Three-Dimensional Grid Generation

The basic idea of three-dimensional grid generation is similar to that of the two-dimensional case. The computational space is a unit cubic with $\xi \in [0,1], \eta \in [0,1], \zeta \in [0,1]$. The parameter space is a unit cubic with $s \in [0,1], t \in [0,1], u \in [0,1]$, see Figure 1.3.

- $s = 0$ at face F_1 and $s = 1$ at face F_2
- s is the normalized arc-length along edges E_1, E_2, E_3 and E_4
- $t = 0$ at face F_3 and $t = 1$ at face F_4
- t is the normalized arc-length along edges E_5, E_6, E_7 and E_8
- $u = 0$ at face F_5 and $t = 1$ at face F_6
- t is the normalized arc-length along edges E_9, E_{10}, E_{11} and E_{12}

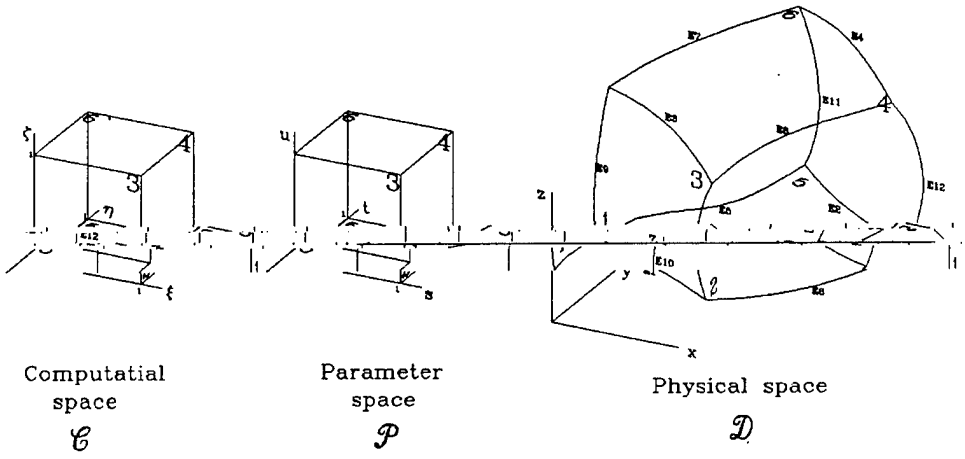

Figure 1.3: Computational space C, Parameter space P, and Physical domain D

Let $s_{E_1}(\xi) = s(\xi,0,0)$, $s_{E_2}(\xi) = s(\xi,1,0)$, $s_{E_3}(\xi) = s(\xi,0,1)$, and $s_{E_4}(\xi) = s(\xi,1,1)$ denote the normalized arc-length along edges E_1, E_2, E_3, and E_4; $t_{E_5}(\eta) = t(0,\eta,0)$, $t_{E_6}(\eta) = t(1,\eta,0)$, $t_{E_7}(\eta) = t(0,\eta,1)$, and $t_{E_8}(\eta) = t(1,\eta,1)$ denote the normalized arc-length along edges E_5, E_6, E_7 and E_8; $u_{E_9}(\zeta) = u(0,0,\zeta)$, $u_{E_{10}}(\zeta) = t(1,0,\zeta)$, $u_{E_{11}}(\zeta) = u(0,1,\zeta)$, and $u_{E_{12}}(\zeta) = u(1,1,\eta)$ denote the normalized arc-length along edges E_9, E_{10}, E_{11} and E_{12}. The algebraic transformation from computational space to parameter space $s : \mathcal{C} \to \mathcal{P}$ is defined as

$$\begin{aligned} s &= s_{E_1}(\xi)(1-t)(1-u) + s_{E_2}(\xi)t(1-u) + s_{E_3}(\xi)(1-t)u + s_{E_4}(\xi)tu \\ t &= t_{E_5}(\eta)(1-s)(1-u) + t_{E_6}(\eta)s(1-u) + t_{E_7}(\eta)(1-s)u + t_{E_8}(\eta)su \\ u &= u_{E_9}(\zeta)(1-s)(1-t) + u_{E_{10}}(\zeta)s(1-t) + u_{E_{11}}(\zeta)(1-s)t + u_{E_{12}}(\zeta)st \end{aligned} \tag{1.12}$$

Equation 1.12 is called the algebraic straight line transformation.

The elliptic transformation $x : \mathcal{P} \to \mathcal{D}$, which is independent of the prescribed boundary grid point distribution, is defined to map the parameter space $\mathcal{P}$ onto the physical domain $\mathcal{D}$. The elliptic transformation is equivalent to a set of Laplace equations

$$\begin{aligned} s_{xx} + s_{yy} + s_{zz} &= 0 \\ t_{xx} + t_{yy} + t_{zz} &= 0 \\ u_{xx} + u_{yy} + u_{zz} &= 0 \end{aligned} \tag{1.13}$$

The elliptic transformation defined by the above equations is also differentiable and one-to-one.

In physical domain, the curvilinear coordinate system satisfies a system of Laplace equations:

$$\Delta \boldsymbol{r} = 0 \tag{1.14}$$

where $\boldsymbol{r} = (x, y, z)^T$.

When the Laplace system Eq.(1.14) is transformed to the computational space C, we obtain a Poisson system:

$$\begin{aligned} & g^{11}\boldsymbol{r}_{\xi\xi} + g^{22}\boldsymbol{r}_{\eta\eta} + g^{33}\boldsymbol{r}_{\zeta\zeta} + 2g^{12}\boldsymbol{r}_{\xi\eta} + 2g^{13}\boldsymbol{r}_{\xi\zeta} + 2g^{23}\boldsymbol{r}_{\eta\zeta} \\ + \; & (g^{11}P^1_{11} + g^{22}P^1_{22} + g^{33}P^1_{33} + 2g^{12}P^1_{12} + 2g^{13}P^1_{13} + 2g^{23}P^1_{23})\boldsymbol{r}_\xi \\ + \; & (g^{11}P^2_{11} + g^{22}P^2_{22} + g^{33}P^2_{33} + 2g^{12}P^2_{12} + 2g^{13}P^2_{13} + 2g^{23}P^2_{23})\boldsymbol{r}_\eta \\ + \; & (g^{11}P^3_{11} + g^{22}P^3_{22} + g^{33}P^3_{33} + 2g^{12}P^3_{12} + 2g^{13}P^3_{13} + 2g^{23}P^3_{23})\boldsymbol{r}_\zeta = 0 \end{aligned} \tag{1.15}$$

where $g^{11}, g^{22}, g^{33}, g^{12}, g^{13}, g^{23}$ are contravariant metric tensor, which are calculated through the covariant metric tensor

$$\begin{aligned} g^{11} &= \frac{1}{J^2}(g_{22}g_{33} - g_{23}^2) \\ g^{22} &= \frac{1}{J^2}(g_{11}g_{33} - g_{13}^2) \\ g^{33} &= \frac{1}{J^2}(g_{11}g_{22} - g_{12}^2) \\ g^{12} &= \frac{1}{J^2}(g_{13}g_{23} - g_{12}g_{33}) \\ g^{13} &= \frac{1}{J^2}(g_{12}g_{23} - g_{13}g_{22}) \\ g^{23} &= \frac{1}{J^2}(g_{12}g_{13} - g_{23}g_{11}) \end{aligned}$$

The control functions are defined through the composite transformation.

$$\begin{aligned} \mathbf{P}_{11} &= -\mathbf{T}^{-1}\begin{pmatrix} s_{\xi\xi} \\ t_{\xi\xi} \\ u_{\xi\xi} \end{pmatrix}, \quad \mathbf{P}_{22} = -\mathbf{T}^{-1}\begin{pmatrix} s_{\eta\eta} \\ t_{\eta\eta} \\ u_{\eta\eta} \end{pmatrix}, \quad \mathbf{P}_{33} = -\mathbf{T}^{-1}\begin{pmatrix} s_{\zeta\zeta} \\ t_{\zeta\zeta} \\ u_{\zeta\zeta} \end{pmatrix} \\ \mathbf{P}_{12} &= -\mathbf{T}^{-1}\begin{pmatrix} s_{\xi\eta} \\ t_{\xi\eta} \\ u_{\xi\eta} \end{pmatrix}, \quad \mathbf{P}_{13} = -\mathbf{T}^{-1}\begin{pmatrix} s_{\xi\zeta} \\ t_{\xi\zeta} \\ u_{\xi\zeta} \end{pmatrix}, \quad \mathbf{P}_{23} = -\mathbf{T}^{-1}\begin{pmatrix} s_{\eta\zeta} \\ t_{\eta\zeta} \\ u_{\eta\zeta} \end{pmatrix} \end{aligned} \tag{1.16}$$

and the matrix $\mathbf{T}$ is defined as

$$\mathbf{T} = \begin{pmatrix} s_\xi & s_\eta & s_\zeta \\ t_\xi & t_\eta & t_\zeta \\ u_\xi & u_\eta & u_\zeta \end{pmatrix} \tag{1.17}$$

The computed grids are in general not orthogonal at the boundary. The algebraic transformation can be redefined in a similar way as in the previous section to obtain a grid which is orthogonal at the boundary. The three-dimensional grid around a delta wing is shown in Figure 1.4.

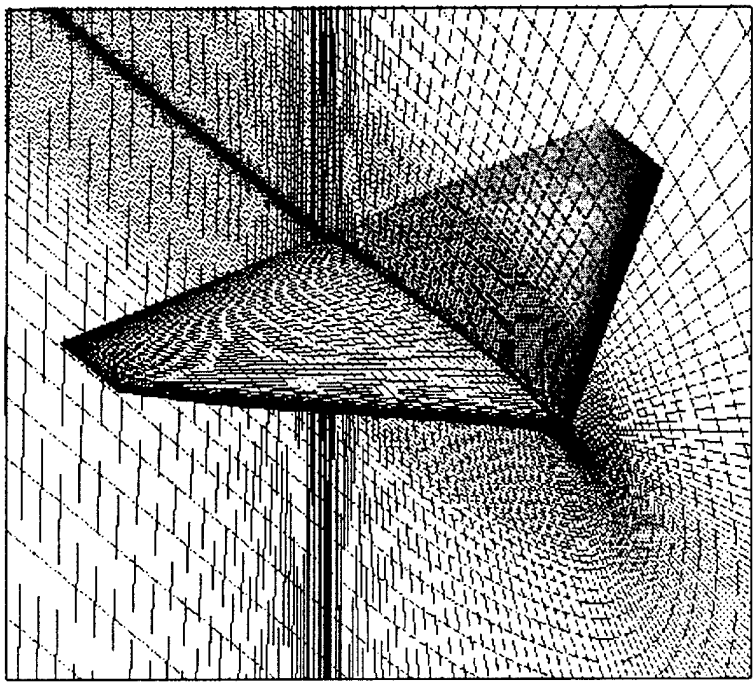

Figure 1.4: Grid around a delta wing

Chapter 2

Parallel Computation

2.1 Introduction

Parallel computing provides an efficient solution for large scale computations, such as direct numerical simulation (DNS) and large eddy simulation (LES), which require both large volume of memory and high speed. In a parallel computer, several processors can work concurrently on various parts of the the same computation. Some parallel computers, such as SGI Origin 2000, have a global memory that can be accessed by all the processors. Such a computer is said to have a share memory. Most programming languages and environments shield the programmer from working directly with processor. Instead they supply a higher lever concept, called a process, that models the activation and a single program on a processor. The shared-memory programming models are characterized by the provision of a global memory that can be directly read from and written to by every process involved in a computation. Compared with a distributed-memory system, a shared-memory computer can provides a larger band-width for communications between different processors.

Two families of programming models have become widely used. High Performance Fortran (HPF) is based on a shared-memory data-parallel model. The other major parallel programming is a distributed-memory model with explicit control parallelism, also referred to as a message passing programming model. Processes in a message passing programming model are only able to read and write into their respective local memory. They synchronize with one another by explicitly calling library procedures. Data is copied across local memories by having the appropriate process send and receive message via explicit procedure of subroutine calls. The Message Passing Interface (MPI) standard defines a set of functions and procedures that implements the message passing model. Although the message passing model was originally designed for the distributed-memory system, it can also be used for a shared-memory system. A message passing model built on a shared-memory infrastructure can achieve a higher speed of data communication because of the larger band-width.

In a shared-memory multi-processor system, such as a SGI Origin 2000 computer, the speed for a processor to access the memory on its node-board (local memory) is different from the speed for it to access the memory of other processor (remote memory). Therefore, even on a shared-memory system, there still will be some overhead caused by data exchange between different processors.

2.2 Parallel Scheme

In our computation, the parallel computing is based on MPI. The computer domain is divided into N_p sub-domains along the ξ direction, where N_p is the number of processes. The data of each sub-domain is stored within the local memory of each processor. Each processor communicates with each other using a group functions provided by MPI library. Data exchange between processors occurs when the data stored in the local memory of other processor is required. For instance, in order to calculate the first and second derivative in the ξ direction using the compact scheme, massive data exchange is achieved by calling the MPI function MPI_ALLTOALL. In some other case, when data exchange is required between the interface of two adjacent sub-domain, the MPI function MPI_SEND and MPI_RECV are used.

2.3 Parallel Speedup

A test code has been used to compare the performance of parallel computing on a SGI Origin 2000 and a Cray T3E. The SGI Origin 2000 is a single large shared-memory system which is also capable to run the MPI code designed for a multiple-instruction multiple-data (MIMD) system. The SGI Origin 2000 we are testing has sixteen R10000 MIPS processors at 250MHz and 4GB of memory.

A MPI code is designed to test the performance of computers. In this testing code, first derivative in ξ, η and ζ directions is computed using the 4th order compact scheme, which is popular high-order scheme in DNS/LES.

The grid numbers in the three direction are 480, 160, and 80 respectively, which represent a moderate scale computation. Several parameters are used to measure the performance of a parallel computing. The wall-clock time is the elapsed time of a MPI program which can be obtained by calling MPI subroutine MPI_WTIME. Speedup is defined as the ratio of the runtime of a serial solution to a problem to the parallel runtime.

$$S(n,p) = \frac{T_\delta(n)}{T_\pi(n,p)} \tag{2.1}$$

where $T_\delta(n)$ denotes the runtime of the serial program running with one process. $T_\pi(n,p)$ denotes the runtime of the parallel code running with p processes.

- $S(n,p) > p$: the parallel program is exhibiting super-linear speedup;
- $S(n,p) = p$: the parallel program is exhibiting linear speedup;
- $1 < S(n,p) < p$: the parallel program is exhibiting speedup;
- $S(n,p) < 1$: the parallel program is exhibiting slowdown;

An alternative to speedup is efficiency, which is a measurement of process utilization in a parallel program, relative to the serial program. It is defined as

$$E(n,p) = \frac{S(n,p)}{p} = \frac{T_\delta(n)}{pT_\pi(n,p)} \tag{2.2}$$

- $E(n,p) > 1$: the parallel program is exhibiting super-linear speedup;
- $E(n,p) = 1$: the parallel program is exhibiting linear speedup;
- $1/p < E(n,p) < 1$: the parallel program is exhibiting speedup;
- $E(n,p) < 1/p$: the parallel program is exhibiting slowdown;

Figure 2.1 presents the wall clock time for 2, 4, 8 16, and 32 processors on Cray T3E. Figure 2.2 shows a similar result obtained on the SGI Origin 2000 computer. On both machines, the wall clock decreases as the number of processors increases. The comparison is displayed in Figure 2.3. The wall clock time to run the same case on T3E is about 2/3 of the time on the Origin 2000 for 2, 4, 8, and 16 processors.

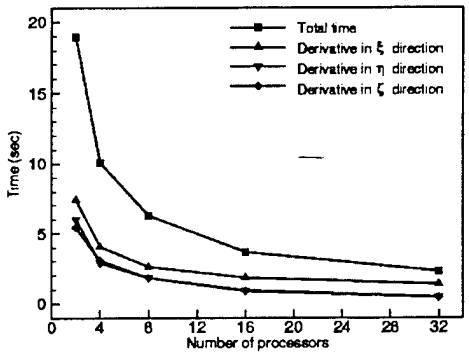

Figure 2.1: Wall-clock time for different number of processors on Cray T3E

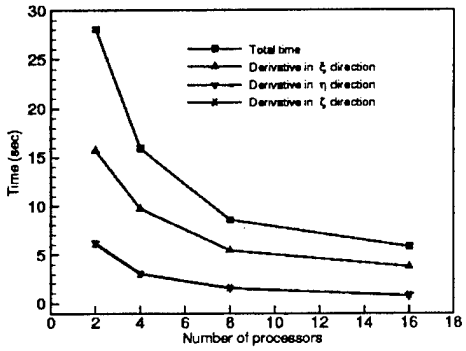

Figure 2.2: Wall-clock time for different number of processors on SGI Origin 2000

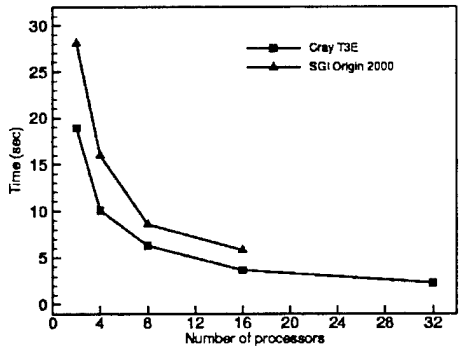

Figure 2.3: Wall-clock time for different number of processors on Cray T3E and SGI Origin 2000

The performances indicated by speedup of MPI code running on T3E and Origin 2000 are displayed in Figure 2.4 and 2.5. The computing of derivative in η and ζ direction display super-linear scalability. Because there is no data exchange in η and ζ direction, the parallel computing is very efficient to calculate derivative in these two directions. On Origin 2000, the super-linear speedup can be explained as following. As the number of processor increase, the ratio between the

cache of each processor and the data handled by the processor also increase, in other words, more data can be put into the cache, which has a faster accessing speed.

But on T3E, only sub-linear result is obtained. When we submitted the testing MPI job on SGI Origin 2000, no other job was running. But our MPI testing code was submitted to T3E running with many jobs submitted by other users, and only wall-clock time has been recorded. The speedup parameter does not display the linear scalability for calculating derivatives in ξ direction, because massive data exchange is required by calling the MPI function MPI_ALLTOALL. The data exchange between different processors has reduced the total performance of parallel computing. This extra cost for parallel computing is inevitable. The speedup curves as a function of number of processors for T3E and Origin are displayed in Figure 2.6. The total speedup of T3E is better than that of Origin 2000.

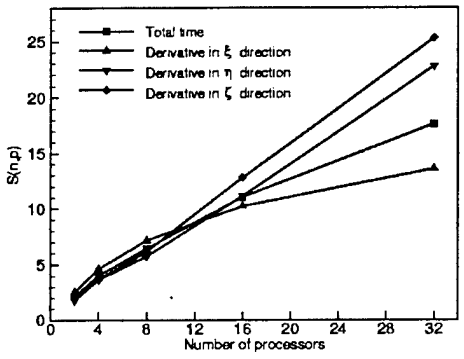

Figure 2.4: Speedup for different number of processors on Cray T3E

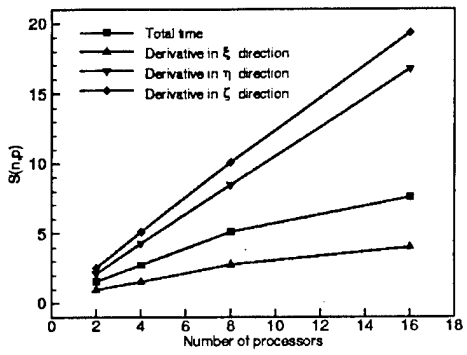

Figure 2.5: Speedup for different number of processors on SGI Origin 2000

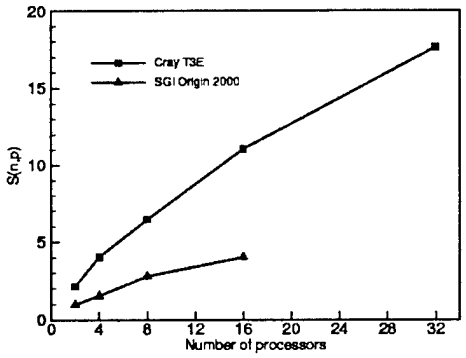

Figure 2.6: Speedup for different number of processors on Cray T3E and SGI Origin 2000

The efficiency parameter are displayed in Figure 2.7 and 2.8. On Cray T3E, when the number of processors is less than 4, the efficiency for calculating derivative in ξ direction and the total performance is greater than 1. That means even the T3E is loaded with jobs submitted from different users, four processors are always available for our job. Therefore, super linear performance is obtained. On Origin 2000, no matter how many processors are used, the efficiency for calculating

derivative in η and ζ direction is always greater than 1, which means super linear performance is attained.

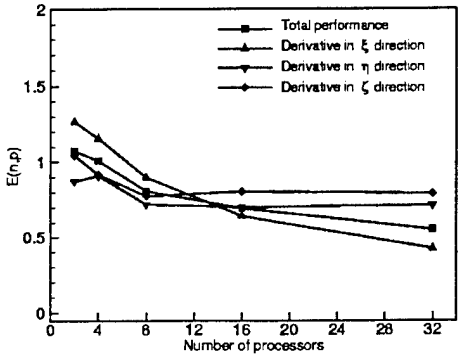

Figure 2.7: Efficiency for different number of processors on Cray T3E

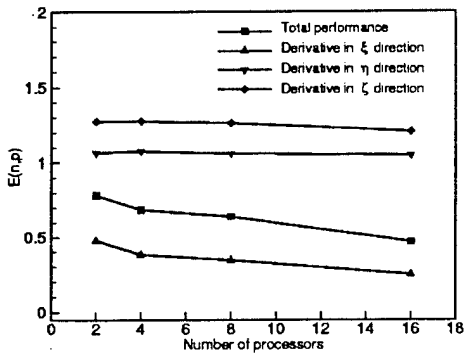

Figure 2.8: Efficiency for different number of processors on SGI Origin 2000

Chapter 3

Numerical Simulation of Separated Flow around a NACA 0012 airfoil at 12° Angle of Attack

3.1 Introduction

It is of particular interest to study the flow separations around airfoils at large angle of attack. Flow separations have at least two effects. The first one is the sudden loss of lift, and the second one is the generation of aerodynamic noise. These two aspects are crucial to the design of aircraft, and these problems can not be solved in the absence of the detailed information about flow separation, which is a complex time-dependent physical process. Understanding of the process is still an open question for research. However, this kind of problem has importance in instantaneous quantities and must studied by DNS or LES at least, but not by RANS (Reynolds-averaged Navier Stokes).

The spatial and temporal complexity of this problem makes it inaccessible by conventional experimental and numerical techniques. From the experimental point of view, as it has been pointed out by Shih *et al.* (1992), that the level of understanding needs to advance from qualitative conjectures based on flow visualization and/or measurement of global quantities, such as lift and drag, to the quantitative measurement of the instantaneous flow field. The prominent feature about the flow past an airfoil at large angles of attack is the emergence of large-scale vortices when the flow separates from the airfoil surface. The spatial and temporal evolution of these vortical structures dominates the unsteady flow behavior over the airfoil. Detailed information, such as spatial vorticity distribution at each instance, is required to study in this problem. This requirement excludes the use of traditional single-point velocity measurement techniques, such as hot-wire anemometry or laser Doppler anemometry. A new experimental technique, particle image displacement velocimetry (PIDV), has been used by Shih *et al.* (1992) to study the unsteady flow past a NACA 0012 airfoil in pitching-up motion in a water towing tank. The Reynolds number based on the airfoil chord and the freestream velocity is 5000. Instantaneous velocity fields at different time have been acquired over the entire 2-D flow field. Using this flow field data, the out-of-plane (spanwise) component of vorticity is computed to show the vortical structures. They found out that boundary-layer separation near the airfoil leading-edge leads to the formation of a vortical structure. Near the leading-edge, vorticity accumulations occurs because of the slowdown of the downstream convection as a result of the adverse pressure gradient. The accumulation process is eventually interrupted by a sudden emergence of unsteady flow separation, with the

immediate release of the accumulated vorticity into the outer flow. This process may be explained by the separation model proposed by Van Dommelen & Shen (1980) and Van Dommelen & Cowley (1990). This model describes the process of initial breakup of unsteady boundary layer through a significant thickening of the boundary layer. In this case, the thickening of boundary layer is driven by the reversing fluid layer which is formed as a result of the adverse pressure gradient. In the reversed flow region, a streamwise accumulation of boundary layer vorticity occurs. The eruption of the boundary layer vorticity lead to formation and shedding of large scale vortical structures which are named as the primary vortices from the leading-edge. The primary vortices move downstream along the airfoil surface and interact with the local boundary layer below to cause the upstream accumulation and eruption of reversal boundary layer vorticity. Near the trailing-edge, the primary vortex further triggers the formation and shedding of a count-rotating vortex. The unsteady separated flow near the leading-edge and trailing edge of a NACA 0012 airfoil was measured in more details by Shih *et al.* (1995) using particle image velocimetry (PIV) technique. In his experiment, the Reynolds number was 5000 and 25000, based on the chord length of the airfoil and the freestream velocity. The role of the trailing edge flow was also examined. At the late stage, as the primary vortex approach the trailing edge, a counter-rotating vortex is shed from the trailing edge. The experimental results obtained by Shih *et al.* (1992, 1995) will be compared with our DNS results in Section 3. It is believed by the authors that the generic characteristics of an unsteady separated flow are fairly universal and independent of the Reynolds number and external flow conditions. The Reynolds number has effect on the time and length scales of the separation structure. For example, the separation structure of a low Reynolds number flow evolves faster than a high Reynolds number case. The stronger viscous diffusion of a low Reynolds number flow will thicken the boundary layer and thereby attenuate the explosive nature of the unsteady separation (Shih *et al.* 1995).

For numerical approaches, Tenaud & Phuoc (1997) used large eddy simulation (LES) to study separated flow around a NACA 0012 airfoil at 20° angle of attack. Three different flow regions following different structure behaviors were observed in their results. The three regions are the leading-edge, the middle part of the upper surface, and the trailing-edge. The leading-edge region is dominated by vortex shedding due to separation of the boundary layer. The second region corresponds to the middle part of the upper surface of the airfoil where the eddy structures grow and are convected downstream. The last region is situated close to the trailing-edge where alternate vortices are created due to the wake instability. The authors did not provide a detailed description of the procedure of vortex shedding from the leading-edge and the subsequent evolution of vortical structures.

This work focuses on direct numerical simulation of flow separation around a NACA 0012 airfoil at a 12° angle of attack. In this case, the following understanding has been obtained from the previous theoretical and experimental investigation. First, the large vortices are intermittently formed and shed from the leading-edge. Second, the separation leads to an alternation of the pressure distribution and therefore changes the lift and moment acting on an airfoil. Thus, the aerodynamic forces become unsteady and there is a dramatic decrease in lift accompanied by an increase in drag and large changes in the moment exerted on the airfoil. Third, the interactions between vortices and between vortices and airfoil surface will generate noise. However, a complete understanding of these complex unsteady effects has not yet been achieved, and there is a great need for systematic fundamental studies. Understanding of flow separation will provide assistance

to improving the separation control and noise control. The main objectives of the present work is to reveal the detailed flow separation structures using high-resolution simulation.

3.2 Governing Equations And Numerical Methods

The two-dimensional Navier-Stokes equations in generalized curvilinear coordinates (ξ, η) are written in conservative forms:

$$\frac{1}{J}\frac{\partial Q}{\partial t} + \frac{\partial (E - E_v)}{\partial \xi} + \frac{\partial (F - F_v)}{\partial \eta} = 0 \tag{3.1}$$

The flux vectors for flow are

$$Q = \begin{pmatrix} \rho \\ \rho u \\ \rho v \\ e \end{pmatrix} \quad E = \frac{1}{J}\begin{pmatrix} \rho U \\ \rho U u + p\xi_x \\ \rho U v + p\xi_y \\ U(e+p) \end{pmatrix}$$

$$F = \frac{1}{J}\begin{pmatrix} \rho V \\ \rho V u + p\eta_x \\ \rho V v + p\eta_y \\ V(e+p) \end{pmatrix} \quad E_v = \frac{1}{J}\begin{pmatrix} 0 \\ \tau_{xx}\xi_x + \tau_{yx}\xi_y \\ \tau_{xy}\xi_x + \tau_{yy}\xi_y \\ q_x\xi_x + q_y\xi_y \end{pmatrix}$$

$$F_v = \frac{1}{J}\begin{pmatrix} 0 \\ \tau_{xx}\eta_x + \tau_{yx}\eta_y \\ \tau_{xy}\eta_x + \tau_{yy}\eta_y \\ q_x\eta_x + q_y\eta_y \end{pmatrix}$$

where J is Jacobian of the coordinate transformation, and $\xi_x, \xi_y, \eta_x, \eta_y$ are coordinate transformation metrics. ρ is density, p is pressure, u and v are components of velocity. $U = u\xi_x + v\xi_y$, $V = u\eta_x + v\eta_y$. e is the total energy. The components of viscous stress and heat flux are denoted by τ_{xx}, τ_{xy}, τ_{yy} and q_x, q_y, respectively.

In Eq. (3.1), the second order Euler Backward scheme is used for time discretization, and the fully implicit form of the discretized equation is:

$$\frac{3Q^{n+1} - 4Q^n + Q^{n-1}}{2J\Delta t} + \frac{\partial (E^{n+1} - E_v^{n+1})}{\partial \xi} + \frac{\partial (F^{n+1} - F_v^{n+1})}{\partial \eta} = 0 \tag{3.2}$$

Q^{n+1} is estimated iteratively as:

$$Q^{n+1} = Q^p + \delta Q^p$$

$$\delta Q^p = Q^{p+1} - Q^p$$

At step $p = 0$, $Q^p = Q^n$; as δQ^p is driven to zero, Q^p approaches Q^{n+1}. Flux vectors are linearized as following:

$$E^{n+1} \approx E^p + A^p \delta Q^p$$

$$F^{n+1} \approx F^p + B^p \delta Q^p$$

So that Eq. (3.2) can be written as:

$$[\frac{3}{2}I + \Delta tJ(D_\xi A + D_\eta B)]\delta Q^p = R \tag{3.3}$$

where R is the residual:

$$R = -(\frac{3}{2}Q^p - 2Q^n + \frac{1}{2}Q^{n-1}) - \Delta tJ[(D_\xi(E - E_v) + D_\eta(F - F_v)]^p$$

The superscript p stands for iteration step. D_ξ, D_η represent partial differential operators, A, B are the Jacobian matrices of flux vectors:

$$A = \frac{\partial E}{\partial Q}, \qquad B = \frac{\partial F}{\partial Q}$$

The right hand side of Eq. (3.3) is discretized using the fourth-order compact scheme (Lele, 1992) for spatial derivatives, and the left hand side of the equation is discretized following LU-SGS method (Yoon & Kwak, 1992). In this method, the Jacobian matrices of flux vectors are split as:

$$A = A^+ + A^-, \quad B = B^+ + B^-$$

where,

$$\begin{aligned} A^\pm &= \frac{1}{2}[A \pm r_A I] \\ B^\pm &= \frac{1}{2}[B \pm r_B I] \end{aligned}$$

where,

$$\begin{aligned} r_A &= \kappa max[|\lambda(A)|] + \tilde{\nu} \\ r_B &= \kappa max[|\lambda(B)|] + \tilde{\nu} \end{aligned}$$

where $\lambda(A), \lambda(B)$ are eigenvalues of A, B respectively, κ is a constant greater than 1. $\tilde{\nu}$ represents the effects of viscous terms. The following expression is used.

$$\tilde{\nu} = max[\frac{\mu}{(\gamma - 1)M_r^2 R_e P_r}, \frac{4}{3}\frac{\mu}{R_e}] \tag{3.4}$$

The first-order upwind finite difference scheme is used for the split flux terms on the left hand side of Eq. (3.3). This does not effect the accuracy of the final solution. As the left hand side is driven to zero, the discretization error of the left hand side will also be driven to zero. The finite difference representation of Eq. (3.3) can be written as:

$$\begin{aligned} &[\frac{3}{2}I + \Delta tJ(r_A + r_B)I]\delta Q^p_{i,j} = \\ &R^p_{i,j} - \Delta tJ\ [A^-\delta Q^p_{i+1,j} - A^+\delta Q^p_{i-1,j} \\ &+B^-\delta Q^p_{i,j+1} - B^+\delta Q^p_{i,j-1}\ ] \end{aligned}$$

In LU-SGS scheme, Eq. (3.5) is solved by three steps. First we initialize δQ^0 using

$$\delta Q^0_{i,j} = [\frac{3}{2}I + \Delta tJ(r_A + r_B)I]^{-1} R^p_{i,j} \tag{3.5}$$

In the second step, the following formula is used:

$$\begin{aligned} \delta Q^*_{i,j} &= \delta Q^0_{i,j} \\ &+ [\frac{3}{2}I + \Delta t J(r_A + r_B)I]^{-1} \\ &\times [\Delta t J(A^+ \delta Q^*_{i-1,j} + B^+ \delta Q^*_{i,j-1})] \end{aligned} \tag{3.6}$$

For the last step, δQ^p is obtained by

$$\begin{aligned} \delta Q^p_{i,j} &= \delta Q^*_{i,j} \\ &- [\frac{3}{2}I + \Delta t J(r_A + r_B)]^{-1} \\ &\times [\Delta t J(A^- \delta Q^p_{i+1,j} + B^- \delta Q^p_{i,j+1})] \end{aligned} \tag{3.7}$$

The sweeping is performed along the planes of $i + j = const$, i.e in the second step, sweeping is from the low-left corner of the grid to the high-right corner, and then vice versa in the third step.

In order to depress numerical oscillation caused by central difference scheme, spatial filtering is used instead of artificial dissipation. The implicit sixth-order compact scheme for space filtering (Lele, 1992) is applied for primitive variables u, v, ρ, p after each time step.

For subsonic flow, u, v, T are prescribed at the upstream boundary, ρ is obtained by solving the modified N-S equation based on characteristic analysis. On the far field and out flow boundary, non-reflecting boundary conditions are applied. Adiabatic, non-slipping condition is used for the wall boundary. All equations of boundary conditions are solved implicitly with internal points. Specific details of boundary treatment can be found in Jiang *et al.* (1999).

3.3 Computational Details

Direct numerical simulation has been implemented to investigate the compressible flow separation around a NACA 0012 airfoil at a 12° angle of attack. The chord length L is taken as the characteristic length, and the freestream velocity U_∞ is the characteristic velocity. The Reynolds number based on the chord length and the freestream velocity is $Re_c = 5 \times 10^5$. The freestream Mach number is 0.4.

An elliptic grid generation method first proposed by Spekreijse (1995) is used to generate the 2-D C-type grids. The elliptic grid generation method is based on a composite mapping, which consists of a nonlinear transfinite algebraic transformation and an elliptic transformation. The algebraic transformation maps the computational space onto a parameter space, and the elliptic transformation maps the parameter space on to the physical domain. The elliptic transformation is carried by solving a set of Poisson equations. The control functions are specified by the algebraic transformation only and it is, therefore, not needed to compute the control functions at the boundary and to interpolate them into the interior of the domain, as required by the well-known elliptic grid generation systems based on Poisson systems (Thompson *et al.*, 1985). The orthogonality of grids on the body surface or near the boundary is attainable by re-configuration of the algebraic transformation.

In Figure 3.1(a), the body-fitted C-grid around a NACA 0012 airfoil is displayed. The mesh near the airfoil surface is shown in Figure 3.1(b) where grids are orthogonal at the boundaries. The mesh is tightened near the wall in the wall-normal direction (η) as well as in the vicinity of the leading- and trailing-edge of the airfoil in the direction parallel to the wall (ξ). The mesh size is 841 points in the ξ direction and 141 points in the η direction.

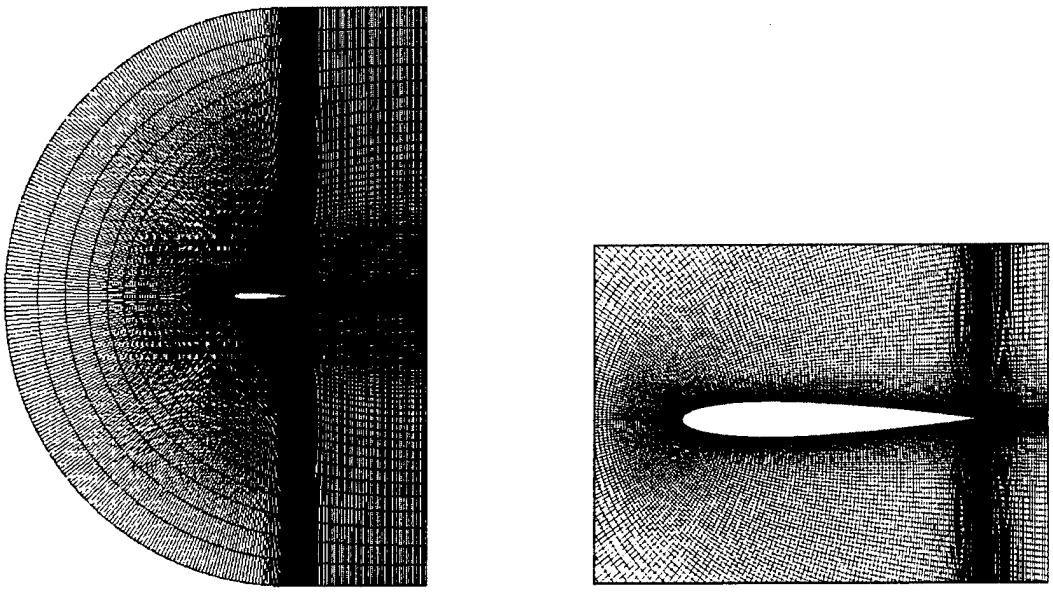

(a) overview of the grids

(b) grid near airfoil surface

Figure 3.1: C-grid around a NACA 0012 airfoil

3.4 Results And Discussions

Flow separations around an airfoil with a high angle of attack ($\alpha = 12°$) has been studied using high-resolution numerical simulation. In this case, the fluid flow around the airfoil becomes very unstable and different eddy structures are formed in the vicinity of the airfoil. These eddy structures severely affect the airfoil's aerodynamic properties. Vortex interactions and the interactions between the airfoil and vortex may lead to noise generation. In the present work, effort is concentrated on providing a detailed picture of flow separation process.

The computation starts from freestream conditions and without any perturbation. During the numerical simulation, the flow separation process is found to be unsteady and the flow field is recorded every 1000 time steps, where the time step is approximately $\Delta t = 1.767 \times 10^{-4} L/U_\infty$. An animation of the flow field has been made based on the recorded data to show the contours of the instantaneous spanwise vorticity. Eighteen snap-shorts with equally spaced time intervals are extracted from the animation and displayed in Figure 3.2. The time interval between two adjacent

frames is about $0.884L/U$. For each frame the region in the vicinity of the trailing-edge are enlarged and displayed in Figure 3.3. In both Figure 3.2 and Figure 3.3, the contours of positive vorticity are plotted in solid lines and negative vorticity are in dotted lines.

In frame (a) of Figure 3.2, instability is observed only in the wake near the trailing-edge of the airfoil. The vicinity of trailing-edge is enlarged and shown in frame (a) of Figure 3.3. Due to the 12° angle of attack, a strong shear layer forms at the trailing edge of the airfoil. The presence of alternate vortices indicates the Kelvin-Helmholtz type instability, which is well-known in the wake where free shear layer appears.

In frame (b) of Figure 3.2, a separation bubble can be observed on the upper surface of the airfoil near the leading-edge. The leading-edge separation bubble is formed when the laminar boundary layer separates from the surface as a result of the strong adverse pressure gradient downstream of the point of minimum pressure. According to the separation model proposed by Van Dommelen & Shen (1980) and Van Dommelen & Cowley (1990), the boundary layer is thickened around the position of vorticity reversal due to streamwise accumulation of fluid driven by the adverse pressure gradient. The accumulation of vorticity eventually leads to the eruption of the boundary layer vorticity and shedding of large scale vortical structures which are named as the primary vortices. The shedding of the primary vortices can be observed in every picture after frame (c) of of Figure 3.2. These vortical structures are rotating in the clockwise direction and with positive spanwise vorticity. A typical case of leading-edge vortex shedding is presented by frame (d) of Figure 3.2 where five vortices are sequently shedding from the leading-edge and moving downstream due to convection. Similar phenomena are captures by the snapshot in frames (i), (l), (m), (q) and (r) of Figure 3.2. Below the primary vortex near the wall, a layer of reversed vorticity is generated due to the induced motion of the primary vortex. As a result, the primary vortices are propelled away from the wall by the reversed vorticity near the surface.

In frame (e) of Figure 3.2, two clockwise rotating primary vortices roll around each other at the middle of the airfoil's upper surface and eventually merge into one large vortex with the original rotating direction. The vortex merging is associated with the adverse pressure gradient along the upper surface of the airfoil. After departure from the leading-edge, the streamwise propagation velocity of the primary vortices is decelerated as a result of the adverse pressure gradient. Therefore, a downstream primary vortex, which leaves the leading-edge earlier and slows down due to the adverse pressure gradient, will be caught up by an upstream vortex which has a larger convective speed. Similar process are seen in frames (h), (o), and (p) of Figure 3.2.

The vortex originated from the the merging of two primary vortices seems to re-attach on the upper surface of the airfoil. It interacts with the local boundary-layer and induces an upstream accumulation and eruption of a reversed boundary-layer vorticity from the wall, see frame (f) of Figure 3.2. In this frame another event of vortex merging is observed near the one-third chord position. The accumulated reversed vorticity leaves the wall as a result of the induced motion by the downstream primary vortex and evolves into a vortex with negative spanwise vorticity, shown in dotted isovorticity contours in frame (f) of Figure 3.2. This induced vortex interacts with the primary vortex to form a counter-rotating vortex pair. A typical vortex pairing phenomenon is presented in frames (g) of Figure 3.2 where two vortex pairs are observed. Similar phenomena of vortex pairing have been described in experiment of Shih *et al.* (1992). The vortex pairs are propelled from the wall by a self-induced motion, whereas they encounter a faster convective motion and move downstream more quickly. At the same time, the vortex pairs experience substantial

deformation due to the difference in streamwise velocity of the main flow close to wall and that far from the wall. Because the far end of the vortex pair moves faster than the near-wall end, the vortex pair is stretched in the streamwise direction, as shown in frame (h) of Figure 3.2. The vortex pair is dominated by the clockwise rotating primary vortex which is stronger than the reversed vortex. And streamwise stretching occurs to the clockwise rotating primary vortex. In frame (h), the downstream vortex pair shown in frame (g) merges with an another vortex pair which comes from the wall. This vortex merging can be seen more clearly in frame (h) of Figure 3.3. In frame (i) of Figure 3.2, all these vortex pairs shown in frame (g) and (h) seem to merge with each other to form a more complex vortex system near the trailing edge of the airfoil.

When the dominating clockwise-rotating part of the vortex system sweeps over the trailing edge of the airfoil, a counterclockwise-rotating vortex which can be seen in frame (h) of Figure 3.3 appears at the trailing-edge. This vortex is named as the trailing-edge vortex, which is generated due to the induced motion of the clockwise-rotating primary vortex. As clockwise-rotating primary vortex reaches the trailing-edge, it introduces a local low pressure region which drives the lower surface of the separating shear layer to curve upward and move across the wake into the upper stream. Then, induced by the clockwise-rotating primary vortex, the shear layer quickly rolls into an intense counterclockwise-rotating trailing-edge vortex. This process is observed clearly in frame (h) and (i) of Figure 3.3. Similar phenomenon was also reported in experiments (Shih *et al.* 1992, 1995).

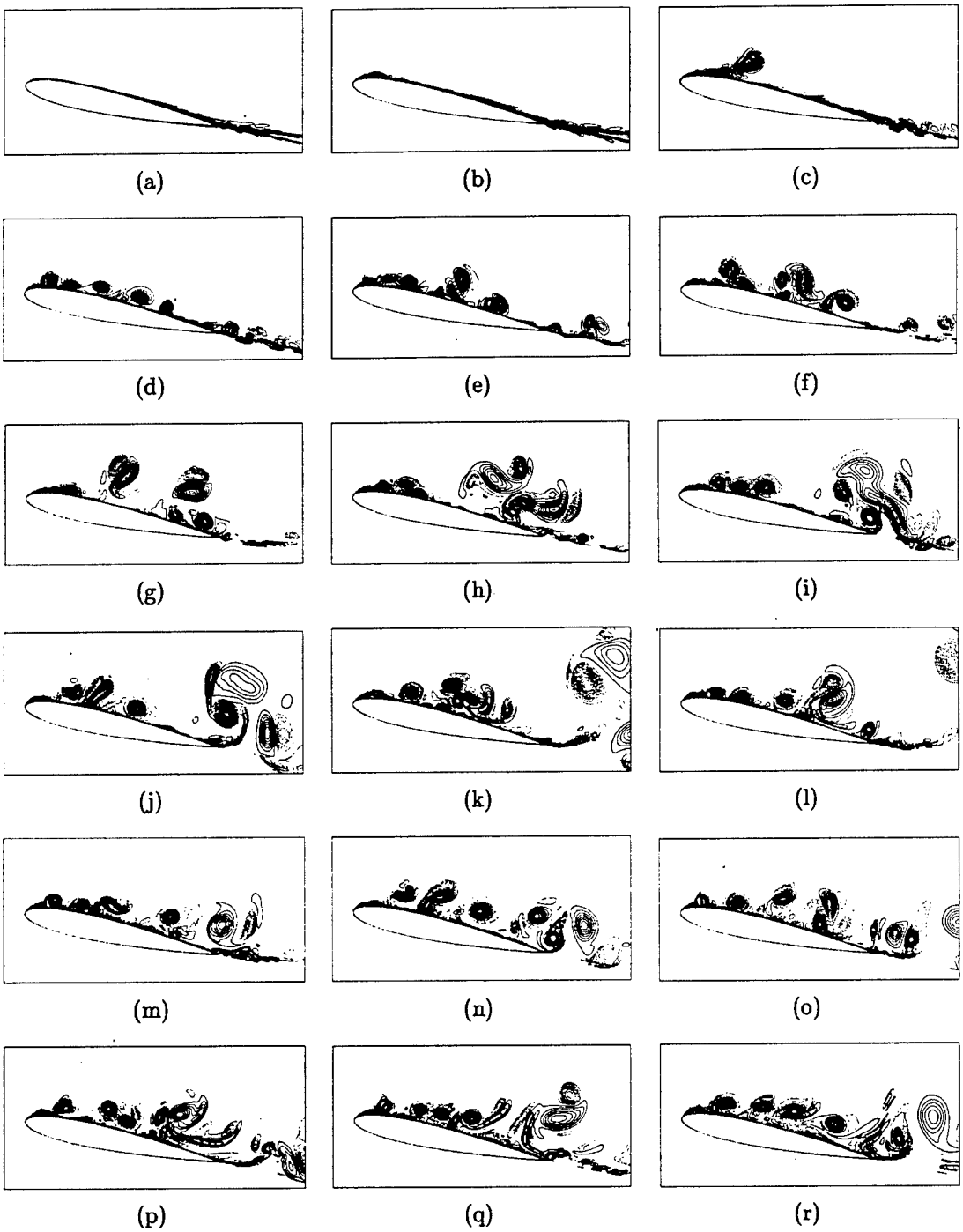

Figure 3.2: Contours of spanwise vorticity at different time. $Re = 5 \times 10^5$, $\alpha = 12°$

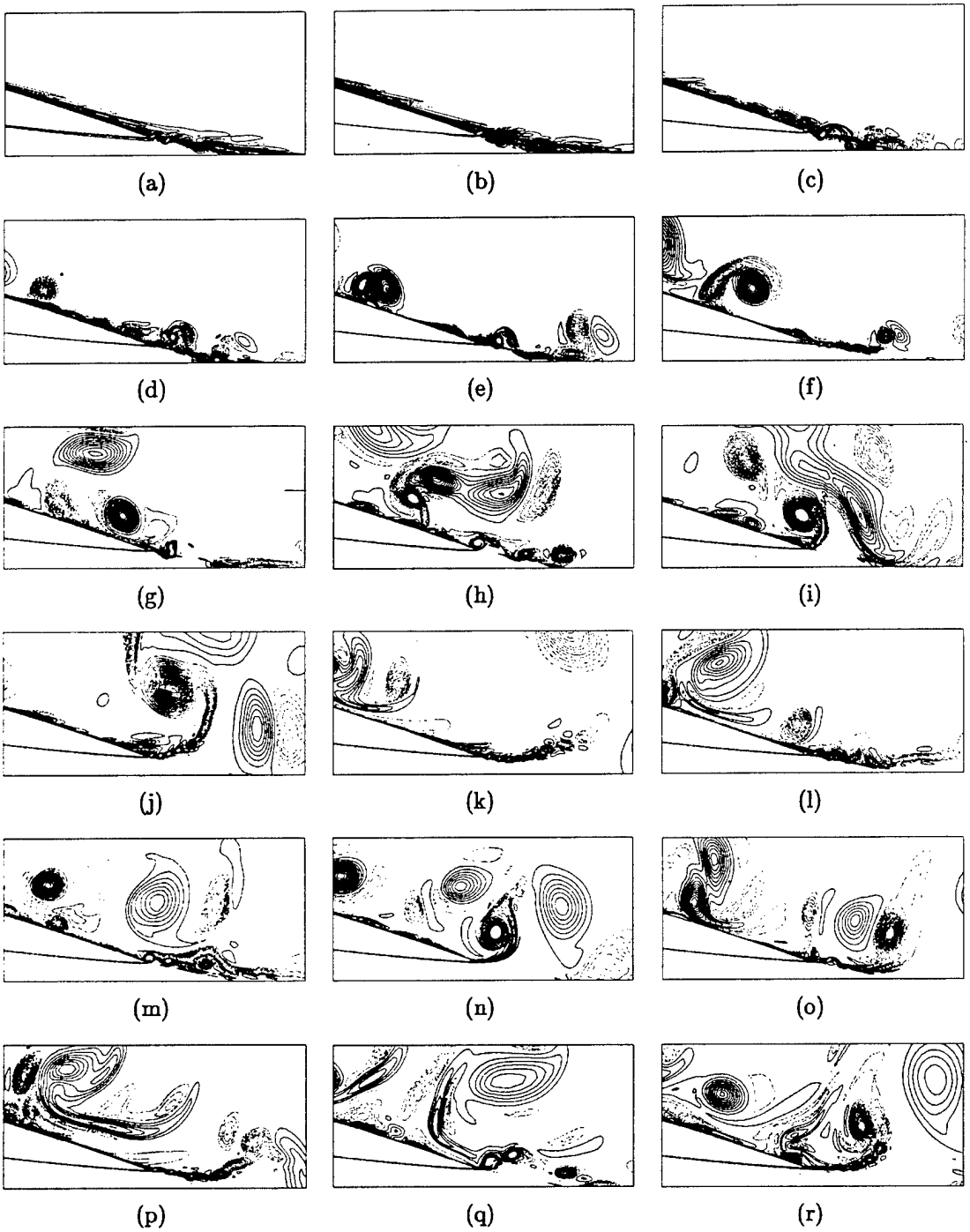

Figure 3.3: Enlarged pictures near the trailing edge for contours of spanwise vorticity at different time. $Re = 5 \times 10^5$, $\alpha = 12°$

In frame (j) of Figure 3.3, the trailing-edge vortex is pushed away from the wall due to a self-induced motion as the vortex grows. The trailing-edge shear layer seems to stick to the downstream edge of the large-scale trailing-edge vortex and is stretched as the trailing-edge vortex is propelled away from the wall. A chain of small-scale counterclockwise-rotating vortical structures appears along the shear layer due to the Kelvin-Helmholtz type instability. Finally the trailing-edge vortex separates from the shear layer to form a vortex pair with a clockwise-rotating primary vortex and diffuses away from the trailing-edge, as shown in frame (j) and (k) of Figure 3.2. As the trailing-edge vortex leaves the trailing edge, pressure recovers near upper surface. Therefore, the shear layer moves back and settles along the streamwise direction, see frames (k) and (l) of Figure 3.3. The Kelvin-Helmholtz type instability structures are still visible along the shear layer until another large-scale primary vortex approaches the trailing-edge and leads to the generation of another trailing-edge vortex.

In the results presented in this paper, the leading-edge vortex continues to shed and convect downstream. Along the upper surface of the airfoil, vortex merging occurs due to the adverse pressure gradient. The leading-edge primary vortex interacts with local boundary layer and triggers reversed vorticity accumulation and eruption, which in turn evolves into the counterclockwise-rotating vortical structures to form vortex pairs with the primary vortex. When these large-scale vortical structures arrive the trailing-edge, a reversed vortical structure is induced from the trailing-edge. This counterclockwise-rotating vortex moves away from the wall by a self-induced motion and separate with the shear layer to interact with the primary vortex and form a vortex pair, which diffuses away from the trailing-edge and moves downstream. Therefore, the generation of the trailing-edge vortex is a quasi-periodic process which can be seen from frame (a) through (r) of Figure 3.2 and Figure 3.3.

To obtain the spectrum information about flow separation, twelve points are selected near the airfoil surface and in the wake to record the time series of instantaneous velocity and pressure. The location of these points are denoted by P1 – P12 and shown in Figure 3.4. Points P1 – P10 locate above and very close to the suction surface of the airfoil. Points P11, P12 are in the wake.

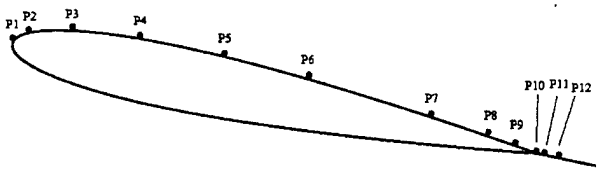

Figure 3.4: Location points P1 – P12 where the time series are recorded

The instantaneous fluctuations of the streamwise velocity and pressure at location point P1 and their power spectrum are displayed in Figure 3.5 – Figure 3.8. Here, the mean flow are defined based on the temporal average. Figure 3.6 shows the power spectrum of streamwise velocity fluctuations, where the first peak associated with the slow variation of mean flow is ignored. The frequency of the second and the third peak is $f = 1.28$, $f = 1.81$. In this case, the vortices shed from the leading edge intermittently, as it can be seen in Figure 3.5, where the high frequency oscillations of u' are linked to vortex shedding. In the spectrum of Figure 3.6, the high frequency is $f = 1.81$, which

reflects the frequency of continuous vortex shedding. The lower $f = 1.28$ is thought to reflect the intermittent feature of vortex shedding. The spectrum of pressure fluctuations exhibit almost the same peak frequency, e.g. $f = 1.28$ and $f = 1.79$.

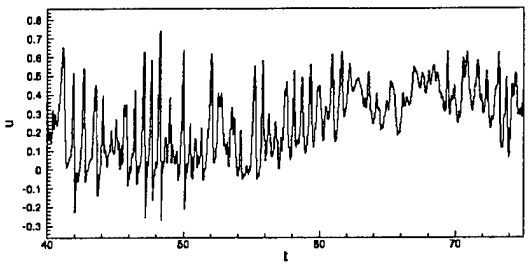

Figure 3.5: Instantaneous streamwise velocity at location point P1

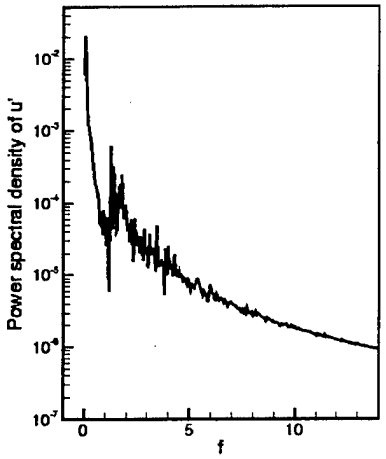

Figure 3.6: Power spectrum density of u' at location point P1

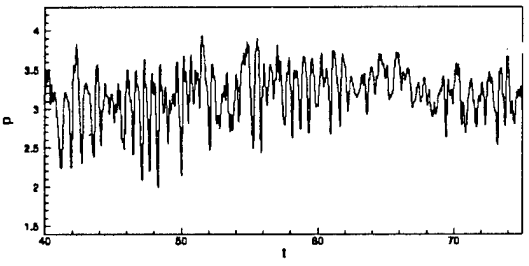

Figure 3.7: Instantaneous pressure at location point P1

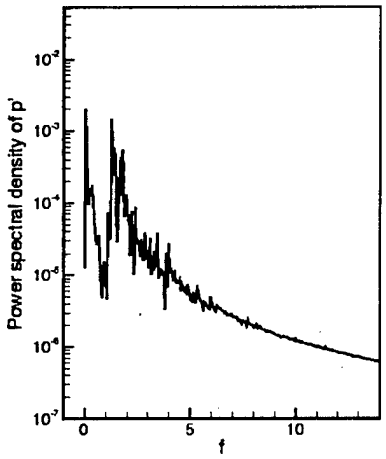

Figure 3.8: Power spectrum density of p' at location point P1

Figure 3.9 – 3.12 show the time series of streamwise velocity, pressure and their spectrums at point P3. At this point, the signals of streamwise velocity and pressure are similar to those at point P1. The frequencies obtained from the velocity and pressure signals are almost the same. The peak frequency is $f = 1.70$, which is close to the vortex shedding frequency at P1.

Figure 3.13 – 3.16 show the time series of streamwise velocity and pressure and their spectrums at point P5. The instantaneous velocity and pressure are more regular compared with those at P1. As a matter of fact, the signals recorded at P5 represent the reattachment of the primary vortex,

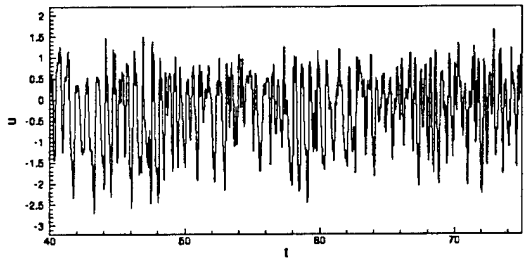

Figure 3.9: Instantaneous streamwise velocity at location point P3

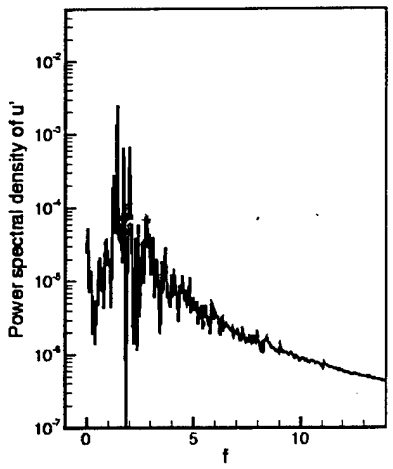

Figure 3.10: Power spectrum density of u' at location point P3

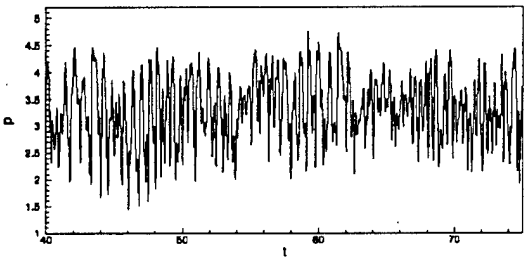

Figure 3.11: Instantaneous pressure at location point P3

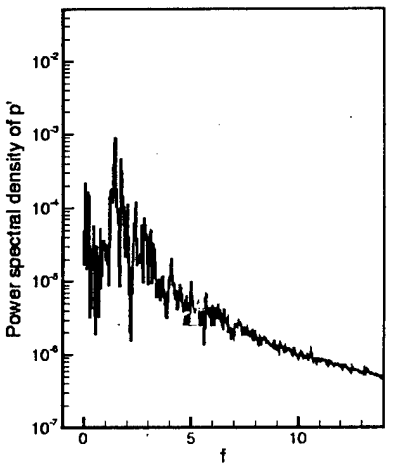

Figure 3.12: Power spectrum density of p' at location point P3

as it is displayed in frames (f) (h) of Figure 3.2. The primary vortices shed from the leading edge rotate clockwise. When a vortex reattaches near point P5, which is close to the wall, the recorded streamwise velocity decrease, while the vortex also causes the pressure to decrease. Therefore, the streamwise velocity signal is in phase with pressure signal, as it is shown in Figure 3.13 and Figure 3.15. In Figure 3.13 and Figure 3.15, the low velocity and low pressure points are corresponding to the vortex reattachment. The frequencies obtained from the velocity and pressure signals are almost the same. The frequency corresponding to the vortex reattachment is $f = 0.29$.

Point P9 locates right above the suction surface near the trailing edge. In Figure 3.3, large scale vortex is found near the trailing edge. The signals recorded at point P9 is used to analyze the

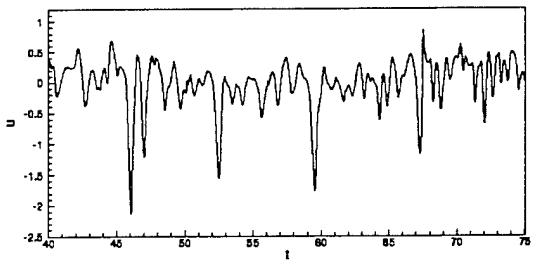

Figure 3.13: Instantaneous streamwise velocity at location point P5

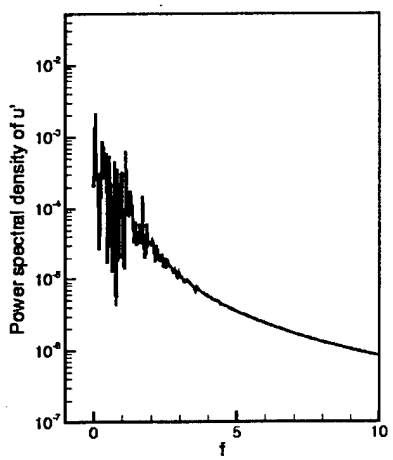

Figure 3.14: Power spectrum density of u' at location point P5

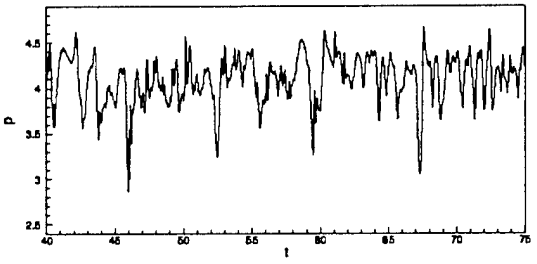

Figure 3.15: Instantaneous pressure at location point P5

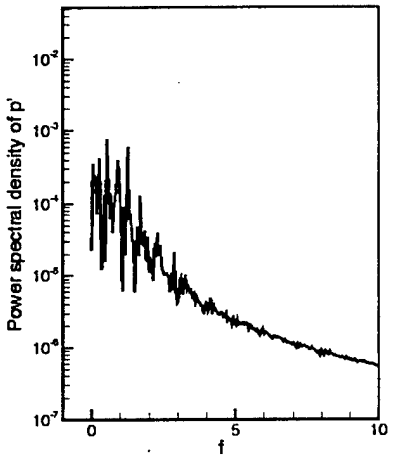

Figure 3.16: Power spectrum density of p' at location point P5

frequency feature of the trailing edge vortex. The instantaneous fluctuations of streamwise velocity and pressure at P9 and their power spectrum are displayed in Figure 3.17 – Figure 3.20. Both the velocity and pressure signals at point P9 are dominated by low-frequency oscillations. It is also interesting to notice that at this point, the streamwise velocity is opposite in phase to pressure; i.e., the streamwise velocity decreases as pressure increases. A brief explanation is given here based on the fact that the trailing vortex rotates counterclockwise. As the trailing vortex appears, at point P9 close to wall, the induced motion of the vortex increases the streamwise velocity, while the pressure decreases. At this point, the peak frequency for velocity is $f = 0.24$ and $f = 0.28$ for pressure.

Now we focus on the next location point P11, which locates in the wake but still close to the

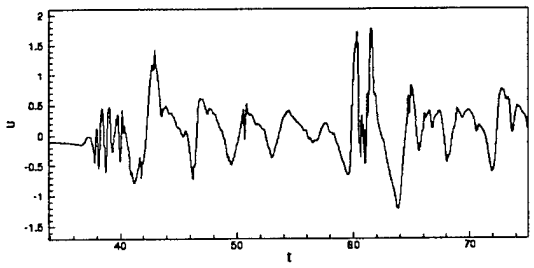

Figure 3.17: Instantaneous streamwise velocity at location point P9

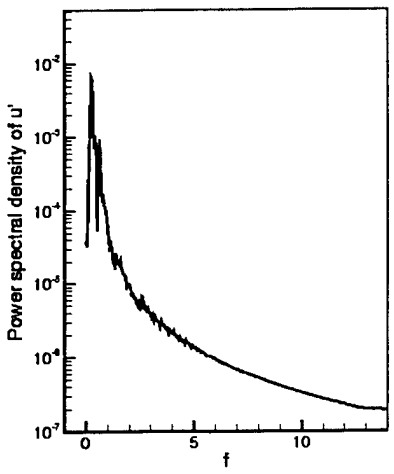

Figure 3.18: Power spectrum density of u' at location point P9

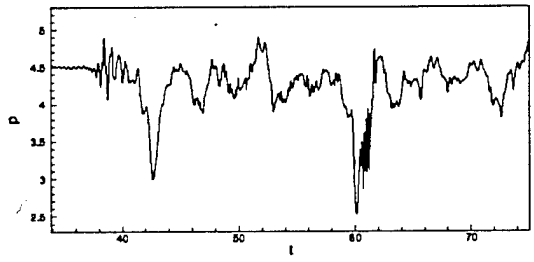

Figure 3.19: Instantaneous pressure at location point P9

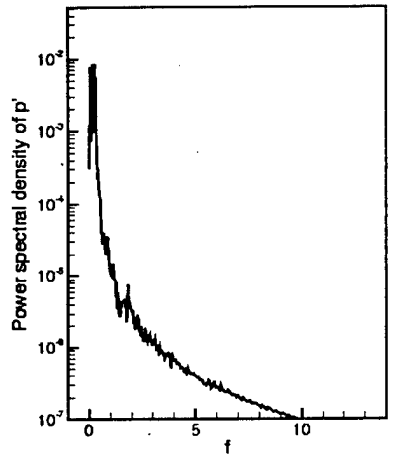

Figure 3.20: Power spectrum density of p' at location point P9

trailing edge. High-frequency oscillations appear on streamwise velocity and pressure displayed in Figure 3.21 and 3.23, respectively. The high-frequency oscillations associated with the small-scale vortex structures appear from the trailing edge along the edge the large-scale trailing edge vortex, as shown in frames (i), (j) (k) of Figure 3.3. The high-frequency parts are modulated by the low-frequency signals corresponding to the large-scale trailing edge vortex.

Point P12 locates at downstream of P11, the signals recorded at initial stage at P12 corresponding to frame (a) to (c) in Figure 3.3 are displayed from Figure 3.25 to Figure 3.28. The regular pattern of the velocity and pressure indicate the typical Kelvin-Helmholtz type instability.

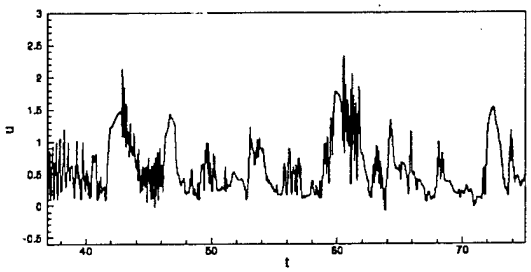

Figure 3.21: Instantaneous streamwise velocity at location point P11

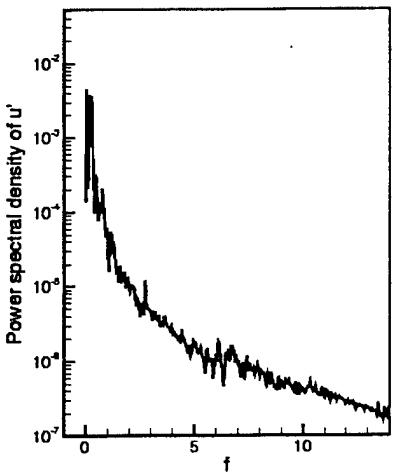

Figure 3.22: Power spectrum density of u' at location point P11

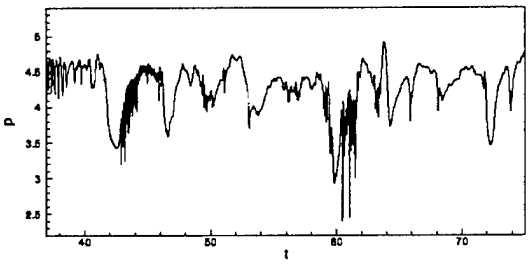

Figure 3.23: Instantaneous pressure at location point P11

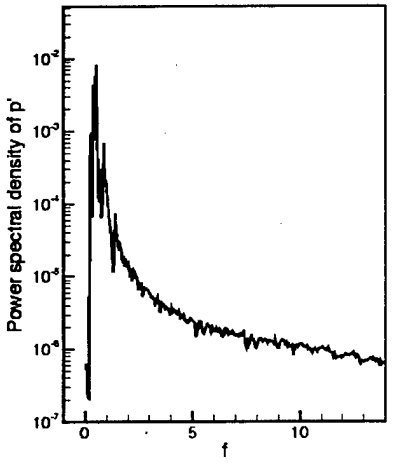

Figure 3.24: Power spectrum density of p' at location point P11

3.5 Conclusions

Direct numerical simulation is carried out by solving the full Navier-Stokes equations in generalized curvilinear coordinates to study the separation flow around a NACA 0012 airfoil at large angle of attack. By using a fourth-order centered compact scheme for spatial discretization, the small-scale vortical structures are resolved, which will dissipate if low-order numerical schemes are used. Non-reflecting boundary conditions are imposed at the far-field and outlet boundaries to avoid possible non-physical wave reflection.

The DNS results clearly describe the flow separation process at the upper surface of the airfoil.

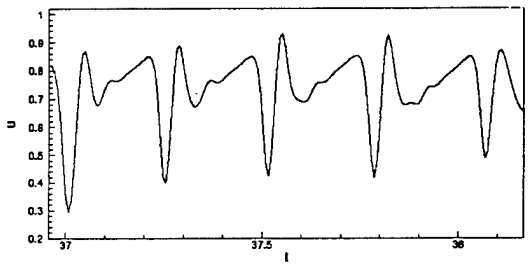

Figure 3.25: Early stage of the instantaneous streamwise velocity at location point P12

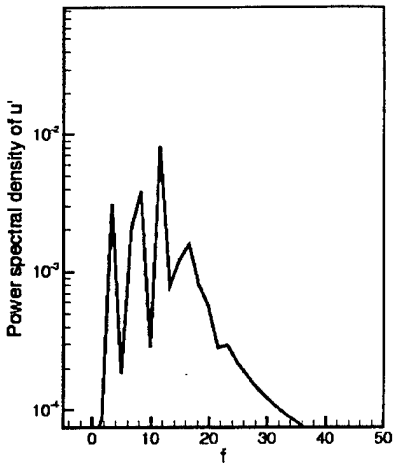

Figure 3.26: Power spectrum density of signal u' in Figure 3.25

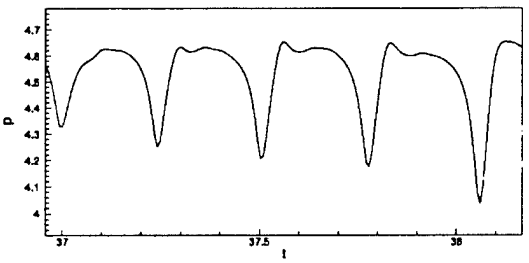

Figure 3.27: Early stage of the instantaneous pressure at location point P12

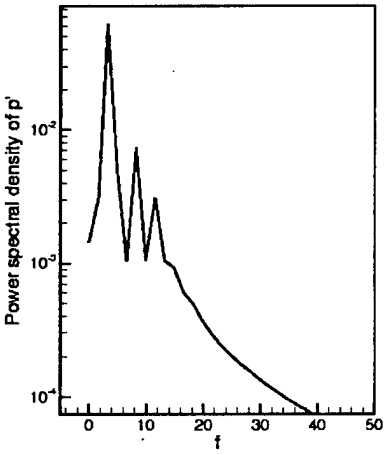

Figure 3.28: Power spectrum density of signal p' in Figure 3.27

The phenomena of the leading-edge separation, vortex shedding, vortex merging, vortex pairing, and formation and shedding of large-scale trailing edge vortex are displayed and discussed in detail. The small-scale vortices associated with the Kelvin-Helmholtz instability are also observed along the shear layer near the trailing-edge. These phenomena are in good agreement with the experimental results obtained by Shih *et al.* (1992, 1995).

Chapter 4

Numerical Simulation of Flow Instability around a Delta Wing

4.1 Introduction

Recent developments in aerospace technology have revived the interest to the study of flow separations around an aircraft maneuvering dynamic operations. Understanding of the complex separated vortical flow is crucial to the aerodynamic design of modern aircraft. Vortical structures, which develop over the leading-edge extension, slender fore-body, and main wing, may have severe effect on the aerodynamic characteristics and performance of modern fighter aircraft.

A flat-plate delta wing with sharp leading-edge provides a simple configuration to investigate the development of the vortical structures. Both experimental and computational results have shown that the flow over the suction side of a delta wing at a fixed angle of attack is dominated by a pair of counter-rotating vortices, i.e. the leading-edge primary vortices. These vortices are formed as a result of the rolling-up of the vortex sheet shedding from the leading-edge. The flow induced by the leading-edge vortices separates near the wing surface and forms a pair of oppositely rotating secondary vortices. The size and strength of the leading-edge vortices increase with the angle of incidence, resulting in a substantial nonlinear lift increment. But the maximum lift of a delta wing is limited by a phenomenon known as vortex breakdown(Visser & Nelson 1993).

In the experimental study using dye visualization carried out by Gad-el-Hak and Balckwelder (1985), small-scale vortices were observed shedding from the leading-edge and feeding into the rolling-up process associated with the large-scale leading-edge vortices. In their study, the small-scale vortices were paired, and were believed as the origination of the classical leading-edge vortices. Payne *et al.* (1988) used smoke flow visualization and laser sheet technique to study the vortical flow field above the delta wing at high angles of attack. Two types of vortex breakdown were testified, i.e. the bubble mode and the spiral mode. In the same experiment, static small-scale vortical-like structures were found in the shear layer of a delta wing with a 85° sweep angle and a 40° angle of attack. The growth of these structures was found to be similar to the evolution of the classic Kelvin-Helmholtz instability. In this experiment, the pairing of the small-scale vortices was not observed. The recent experimental work of Rieley & Lowson (1998) revealed, using flow visualization and hot-wire measurement, the existence of static small vortical structures in the free shear layer shedding from the sharp leading-edge of a delta wing. A local three-dimensional

Kelvin-Helmholtz-type instability was suggested by the authors for the formation of these vortical structures in the free shear layer. Similar vortical structures were also observed in the investigations of Cipolla & Rockwell (1998), where small-scale concentrations of vorticity form near the leading-edge of a rolling delta wing. These vortices appear to evolve in a coupled fashion, which has been considered as the wake-like instability.

Numerical simulations of vortex breakdown above a stationary sharp edged delta wing over a range of angles of attack were carried out by Modiano & Murman (1994). Their computation was based on an Euler solver with adaptive mesh system. The spiral form of vortex breakdown was observed without the emergence of the small-scale vortical structures inside the shear layer. In the numerical investigation by Argwal *et al.* (1992), the well-known Euler/Navier-Stokes code CFL3D was used to simulate the leading-edge vortex breakdown of a low-speed flow on a flat-plate delta wing with sharp leading-edges. Although the vortex breakdown positions obtained from the computation were reported in good agreement with experimental data, the small-scale vortices were not observed, which could be attributed to the lack of numerical resolution/accuracy. A numerical investigation of the unsteady vortex structure over a 76° sweep wing at 20.5° angle of attack was carried out by Gordnier & Visbal (1994). Their numerical calculation indicated that the small-scale vortical structures emanated from the leading-edge was brought on by the Kelvin-Helmholtz-type instability. Pairing of the small vortices was not observed in the computational results.

The intention of present work is to study the mechanism of vortex breakdown above a slender flat-plate delta wing with sharp leading-edges at a fixed angle of attack. Direct numerical simulation is employed to give a detailed description of flow instability and vortex shedding near the leading-edge of the delta wing.

4.2 Governing Equations

The three-dimensional compressible Navier-Stokes equations in generalized curvilinear coordinates (ξ, η, ζ) are written in conservative forms:

$$\frac{1}{J}\frac{\partial Q}{\partial t} + \frac{\partial (E - E_v)}{\partial \xi} + \frac{\partial (F - F_v)}{\partial \eta} + \frac{\partial (G - G_v)}{\partial \zeta} = 0 \tag{4.1}$$

The flux vectors for compressible flow are

$$Q = \begin{pmatrix} \rho \\ \rho u \\ \rho v \\ \rho w \\ e \end{pmatrix}$$

$$E = \frac{1}{J}\begin{pmatrix} \rho U \\ \rho U u + p\xi_x \\ \rho U v + p\xi_y \\ \rho U w + p\xi_z \\ U(e+p) \end{pmatrix}$$

$$
\begin{aligned}
F &= \frac{1}{J}\begin{pmatrix} \rho V \\ \rho V u + p\eta_x \\ \rho V v + p\eta_y \\ \rho V w + p\eta_z \\ V(e+p) \end{pmatrix} \\
G &= \frac{1}{J}\begin{pmatrix} \rho W \\ \rho W u + p\zeta_x \\ \rho W v + p\zeta_y \\ \rho W w + p\zeta_z \\ W(e+p) \end{pmatrix} \\
E_v &= \frac{1}{J}\begin{pmatrix} 0 \\ \tau_{xx}\xi_x + \tau_{yx}\xi_y + \tau_{zx}\xi_z \\ \tau_{xy}\xi_x + \tau_{yy}\xi_y + \tau_{zy}\xi_z \\ \tau_{xz}\xi_x + \tau_{yz}\xi_y + \tau_{zz}\xi_z \\ q_x\xi_x + q_y\xi_y + q_z\xi_z \end{pmatrix} \\
F_v &= \frac{1}{J}\begin{pmatrix} 0 \\ \tau_{xx}\eta_x + \tau_{yx}\eta_y + \tau_{zx}\eta_z \\ \tau_{xy}\eta_x + \tau_{yy}\eta_y + \tau_{zy}\eta_z \\ \tau_{xz}\eta_x + \tau_{yz}\eta_y + \tau_{zz}\eta_z \\ q_x\eta_x + q_y\eta_y + q_z\eta_z \end{pmatrix} \\
G_v &= \frac{1}{J}\begin{pmatrix} 0 \\ \tau_{xx}\zeta_x + \tau_{yx}\zeta_y + \tau_{zx}\zeta_z \\ \tau_{xy}\zeta_x + \tau_{yy}\zeta_y + \tau_{zy}\zeta_z \\ \tau_{xz}\zeta_x + \tau_{yz}\zeta_y + \tau_{zz}\zeta_z \\ q_x\zeta_x + q_y\zeta_y + q_z\zeta_z \end{pmatrix}
\end{aligned}
$$

where J is Jacobian of the coordinate transformation, and $\xi_x, \xi_y, \xi_z, \eta_x, \eta_y, \eta_z, \zeta_x, \zeta_y, \zeta_z$ are coordinate transformation metrics. τ_{kl}'s and q_k's are the viscous stress and the heat flux, respectively.

In Eq. (4.1), second order Euler Backward scheme is used for time derivatives, and the fully implicit form of the discretized equations is:

$$
\begin{aligned}
&\frac{3Q^{n+1} - 4Q^n + Q^{n-1}}{2J\Delta t} + \frac{\partial(E^{n+1} - E_v^{n+1})}{\partial\xi} \\
&+ \frac{\partial(F^{n+1} - F_v^{n+1})}{\partial\eta} + \frac{\partial(G^{n+1} - G_v^{n+1})}{\partial\zeta} = 0
\end{aligned}
\tag{4.2}
$$

Q^{n+1} is estimated iteratively as:

$$
Q^{n+1} = Q^p + \delta Q^p \tag{4.3}
$$

where,

$$
\delta Q^p = Q^{p+1} - Q^p \tag{4.4}
$$

At step $p = 0$, $Q^p = Q^n$; as δQ^p is driven to zero, Q^p approaches Q^{n+1}. Flux vectors are linearized as follows:

$$
E^{n+1} \approx E^p + A^p \delta Q^p
$$

$$F^{n+1} \approx F^p + B^p \delta Q^p \tag{4.5}$$
$$G^{n+1} \approx G^p + C^p \delta Q^p$$

So that Eq. (4.2) can be written as:

$$[\frac{3}{2}I + \Delta t J(D_\xi A + D_\eta B + D_\zeta C)]\delta Q^p = R \tag{4.6}$$

where R is the residual:

$$\begin{aligned} R &= -(\frac{3}{2}Q^p - 2Q^n + \frac{1}{2}Q^{n-1}) - \Delta t J[(D_\xi(E - E_v) \\ &+ D_\eta(F - F_v) + D_\zeta(G - G_v)]^p \end{aligned}$$

D_ξ, D_η, D_ζ represent partial differential operators, and A, B, C are the Jacobian matrices of flux vectors:

$$A = \frac{\partial E}{\partial Q}, \quad B = \frac{\partial F}{\partial Q}, \quad C = \frac{\partial G}{\partial Q} \tag{4.7}$$

The right hand side of Eq. (4.6) is discretized using fourth-order compact scheme (Lele, 1992) for spatial derivatives, and the left hand side of the equation is discretized following LU-SGS method (Yoon & Kwak, 1992). In this method, the Jacobian matrices of flux vectors are split as:

$$A = A^+ + A^-, \quad B = B^+ + B^-, \quad C = C^+ + C^-$$

where,

$$\begin{aligned} A^\pm &= \frac{1}{2}[A \pm r_A I] \\ B^\pm &= \frac{1}{2}[B \pm r_B I] \\ C^\pm &= \frac{1}{2}[C \pm r_C I] \end{aligned} \tag{4.8}$$

and,

$$\begin{aligned} r_A &= \kappa max[|\lambda(A)|] + \tilde{\nu} \\ r_B &= \kappa max[|\lambda(B)|] + \tilde{\nu} \\ r_C &= \kappa max[|\lambda(C)|] + \tilde{\nu} \end{aligned}$$

where $\lambda(A), \lambda(B), \lambda(C)$ are eigenvalues of A, B, C respectively, κ is a constant greater than 1. $\tilde{\nu}$ is taken into account for the effects of viscous terms, and the following expression is used:

$$\tilde{\nu} = max[\frac{\mu}{(\gamma - 1)M_r^2 R_e P_r}, \frac{4}{3}\frac{\mu}{R_e}]$$

The first-order upwind finite difference scheme is used for the split flux terms in the left hand side of Eq. (4.6). This does not effect the accuracy of the scheme. As the left hand side is driven to zero, the discretization error will also be driven to zero. The finite difference representation of Eq. (4.6) can be written as:

$$\begin{aligned} [\frac{3}{2}I &+ \Delta t J(r_A + r_B + r_C)I]\delta Q^p_{i,j,k} = R^p_{i,j,k} \\ -\Delta t J \quad [\quad & A^-\delta Q^p_{i+1,j,k} - A^+\delta Q^p_{i-1,j,k} \\ &+ B^-\delta Q^p_{i,j+1,k} - B^+\delta Q^p_{i,j-1,k} \\ &+ C^-\delta Q^p_{i,j,k+1} - C^+\delta Q^p_{i,j,k-1} \quad] \end{aligned} \tag{4.9}$$

In LU-SGS scheme, Eq. (4.9) is solved by three steps. First initialize δQ^0 using

$$\delta Q^0_{i,j,k} = [\frac{3}{2}I + \Delta t J(\tau_A + \tau_B + \tau_C)I]^{-1} R^p_{i,j,k}$$

In the second step, the following relation is used:

$$\delta Q^*_{i,j,k} = \delta Q^0_{i,j,k} + [\frac{3}{2}I + \Delta t J(\tau_A + \tau_B + \tau_C)I]^{-1}$$
$$\times[\Delta t J(A^+ \delta Q^*_{i-1,j,k} + B^+ \delta Q^*_{i,j-1,k} + C^+ \delta Q^*_{i,j,k-1})]$$

For the last step, δQ^p is obtained by

$$\delta Q^p_{i,j,k} = \delta Q^*_{i,j,k} - [\frac{3}{2}I + \Delta t J(\tau_A + \tau_B + \tau_C)]^{-1}$$
$$\times[\Delta t J(A^- \delta Q^p_{i+1,j,k} + B^- \delta Q^p_{i,j+1,k} + C^- \delta Q^p_{i,j,k+1})]$$

The sweeping is performed along the planes of $i+j+k = const$, i.e. in the second step, sweeping is from the low-left corner of the grid to the high-right corner, and then vice versa in the third step.

In order to depress numerical oscillation caused by central difference scheme, spatial filtering is used instead of artificial dissipation. Implicit sixth-order compact scheme for space filtering (Lele, 1992) is applied for primitive variables u, v, w, ρ, p after each time step.

For subsonic flow, u, v, w, T are prescribed at the inflow boundary, ρ is obtained by solving modified N-S equation based on the characteristic analysis. On the far field and out flow boundary, non-reflecting boundary conditions are applied. Adiabatic, non-slipping conditions are used for the wall boundary. All equations of boundary conditions are solved implicitly with internal points. Specific details of boundary treatment can be found in Jiang *et al* (1999).

4.3 Computational Details

Direct numerical simulation has been implemented to investigate the compressible flow separation around a slender delta wing. The geometry of the delta wing, taken from the experimental work of Rieley & Lowson (1998), is shown in Figure 4.1. The sweep angle denoted by Λ is 80° and the leading-edge angle denoted by σ is 30°. The chord length is taken as the characteristic length L, such that the non-dimensional chord length is $c = 1.0L$. The non-dimensional thickness of the delta wing is $h = 0.024L$. The freestream velocity U_∞ is the characteristic velocity.

An H-C type mesh system for a half-plane model of the delta wing is used based on the assumption that the flow is symmetrical to the the half-plane. The mesh is H-type in the meridian section and C-type in the cross section. An elliptic grid generation method, first proposed by Spekreijse (1995), is used to generate the three-dimensional grids. This method is based on a composite mapping, which is consisted of a nonlinear transfinite algebraic transformation and an elliptic transformation. The grids are orthogonal on the delta wing surface. The sharp leading-edge is approximated by a round edge with a small radius of $1.0 \times 10^{-3}L$, while in the experiment of Rieley & Lowson (1998), the average thickness of the leading-edge was 0.12 mm, which was approximately $2.55 \times 10^{-4}L$. Computations are carried out on two grid systems, i.e. the low resolution mesh with $140 \times 70 \times 70$ grid nodes and the high resolution mesh with $180 \times 150 \times 70$ grid nodes,

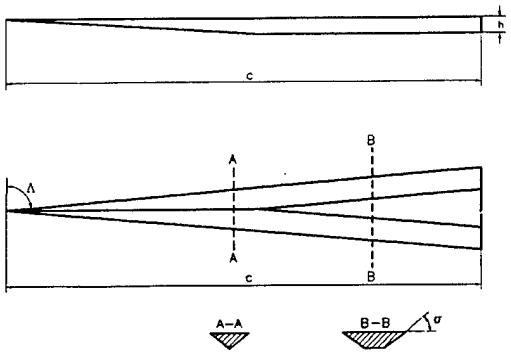

Figure 4.1: Schematic of the delta wing

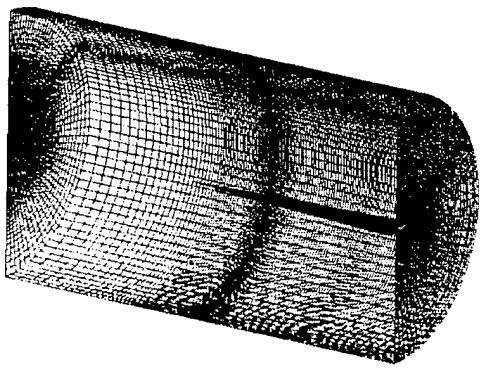

Figure 4.2: H-C type grid around a 85° sweep delta wing

where the sequence of numbers is corresponding to the axial, the spanwise and the wall-normal direction, respectively. An example of the three-dimensional grid is displayed in Figure 4.2.

The parallel version of the DNS code based on the Message Passing Interface (MPI) has been developed to accelerate the computation. Although massive data exchanges are required for computing the derivatives with the compact finite difference scheme, the speedup is still substantial. On a SGI Origin 2000 computer, the performance of the MPI code is superior to the serial code, which is compiled using the automatic parallelization option provided by Fortran 90 compiler. The comparison are displayed in Figure 4.3, where the speedup parameter $S(n,p)$ is defined as the ratio of the runtime of a serial solution to a problem to the parallel runtime. Linear speedup has been achieved for MPI code running on 4, 6, and 15 processors. The final parallel computation for the higher Reynolds number case with a mesh of $180 \times 150 \times 70$ is conducted using 10 processors on a SGI Origin 2000 computer.

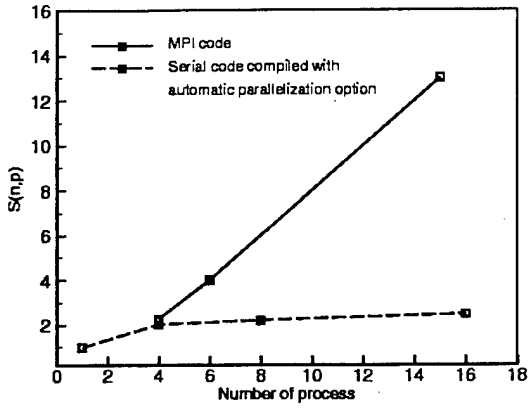

Figure 4.3: Speedup $S(n,p)$ of the MPI code compared with the serial code complied with automatic parallelization option

4.4 Results and Discussions

4.4.1 Low Reynolds number case

All results presented here are obtained from direct numerical simulation of flow around a 85° sweep delta wing with a flat-plate suction surface, which has been introduced in Section 3. The angle of attack is fixed at 12.5°. The free-stream Mach number is $Ma = 0.1$. For the lower resolution simulation, the Reynolds number based on the chord length and the free-stream velocity is $Re_c = 5 \times 10^4$. No initial and boundary disturbance are imposed in the simulation.

The contours of the axial vorticity on selected cross sections are displayed in Figure 4.4. It is quite clear that a pair of counter-rotating vortices, so called the leading-edge primary vortices, appears over the suction side of the delta wing. These vortices form as a result of flow separation and the rolling-up of the vortex sheet shedding from the leading-edge. The primary vortices are steady and stable in this low Reynolds number case. The primary vortices are composed of a pair of counter-rotating oblique vortex tubes starting from the apex of delta wing, from a three-dimensional point of view. Beneath the primary vortices, near the upper surface of the delta wing, the secondary vortices, which have an opposite rotating direction to the primary vortices, are formed as a result of the spanwise outflow induced by the primary vortex. Figure 4.5 shows the three-dimensional instantaneous streamlines starting from vicinity of the leading-edge. The streamlines also reveals the existence of the cone-shaped primary vortices. The computational results are in good agreement with the experimental results of Riley & Lowson (1998). During the computation for the high Reynolds number case, the flow becomes unsteady and small-scale vortical structures keep shedding from the leading-edge. In the experiment of Riley & Lowson (1998), flow instability was observed when the Reynolds number was raised above $Re_c = 100,000$. In order to study the flow instability near the leading edge, the numerical simulation with a higher resolution and higer Reynolds number has been implemented, and the results are discussed in next section.

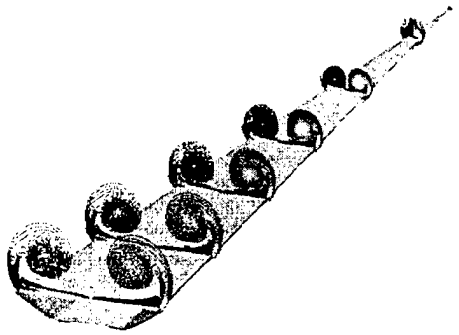

Figure 4.4: Contours of the axial vorticity on selected cross sections, angle of attack $\alpha = 12.5°$, $Re = 5 \times 10^4$, $Ma = 0.1$

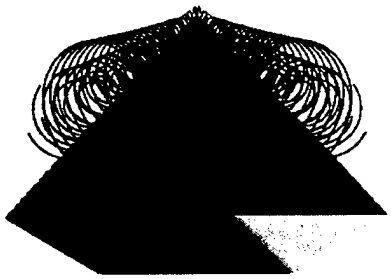

Figure 4.5: Three-dimensional streamline above the suction surface of a 85° sweep delta wing at an angle of attack $\alpha = 12.5°$, $Re = 5 \times 10^4$, $Ma = 0.1$

4.4.2 High Reynolds number case

At higher Reynolds number, i.e. $Re_c = 1.96 \times 10^5$, which is the same as the one chosen by Riley & Lowson (1998) in their experimental study, where the flow instability occurs near the leading edge of the delta wing. In order to capture the small vortical structures observed in the experiment, the numerical simulation is accomplished on a mesh with a higher resolution of $180 \times 150 \times 70$. During the simulation, flow instability and periodic shedding of small vortical structures are observed. Since there is no disturbance imposed as the initial or boundary condition for the computation, the unstable behavior presented by the flow in the computational results are rather intrinsic.

The distributions of the instantaneous axial vorticity on various cross sections are shown in Figure 4.6. Compared with the low Reynolds number results of Figure 4.4, the flow is still dominated by a pair of primary vortices. But instability appears at the leading-edge of delta wing, where vortex shedding is observed. On the suction surface near the leading-edge, the secondary vortices are still visible in this figure.

In Figure 4.7 the contours of axial vorticity at different time on a cross section at $x = 0.87L$ are displayed through (a) to (h), each frame is corresponding to a snapshot of a two-dimensional flow field at a certain time. Flow instability is quite obvious in these figures. The primary vortex deforms compared to the low Reynolds number case. The flow pattern inside the primary vortex resembles that of the spiral instability mode, which presented occasionally in the experiment of Rieley & Lowson(1998). Two strong shear layers are visible through the concentration of axial vorticity contours. The first one is the leading-edge shear layer whose axial vorticity is positive (shown in light color in Figure 4.7), which wraps the leading-edge corner from below and feeds into the primary vortex. The other one lies between the primary vortex and the upper surface of the delta wing and has a negative axial vorticity (shown in dark color in Figure 4.7), which is associated with the secondary vortex. Therefore, the shear layer below the primary vortex is also called the secondary shear layer. As it will be discussed later, both the leading-edge shear layer

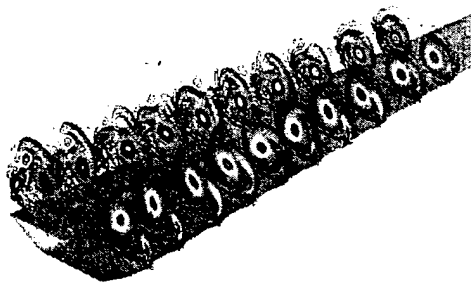

Figure 4.6: The instantaneous distributions of the axial vorticity on various cross sections. Angle of attack $\alpha = 12.5°$, $Re = 1.96 \times 10^5$, $Ma = 0.1$

and the secondary shear layers are related to the instability and vortex shedding procedure near the leading-edge.

Among the small-scale vortical structures shedding from the leading-edge, there are two types of vortices, distinguished by the direction of rotation or by the sign of axial vorticity. Those vortices whose rotating direction is the same as the primary vortex are named as the A-family vortices, which are corresponding to a positive axial vorticity component. The vortices rotating in the opposite direction as the primary vortex are called the B-family vortices and have a negative axial vorticity component. The A-family vortices are much stronger than the B-family vortices, which can be recognized from the contours of the axial vorticity in Figure 4.7.

In Figure 4.7(a), a bulge is observed on the leading-edge shear layer. The bulge grows in size as it moves away from the leading edge, as shown in Figure 4.7(b), (c), and (d). This process is corresponding to the generation and shedding of the A-family vortex. Because the B-family vortices are very weak, the shedding process of B-family vortices is not clear in Figure 4.7. A more detailed study reveals that the B-family vortex comes from the shedding of the secondary vortex.

(a) $t = 55.54L/U_\infty$

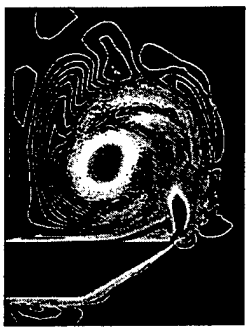

(b) $t = 55.68L/U_\infty$

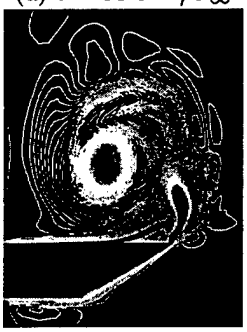

(c) $t = 55.81L/U_\infty$

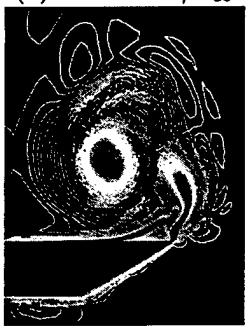

(d) $t = 55.95L/U_\infty$

(e) $t = 56.09L/U_\infty$

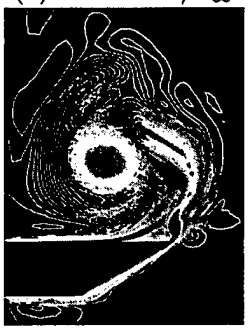

(f) $t = 56.23L/U_\infty$

(g) $t = 56.37L/U_\infty$

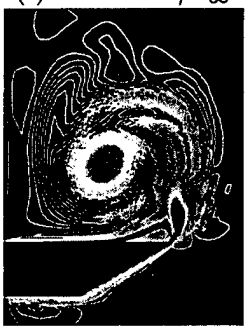

(h) $t = 56.51L/U_\infty$

Figure 4.7: Contours of axial vorticity of different time on a cross section at $x = 0.87L$. Angle of attack $\alpha = 12.5°$, $Re = 1.96 \times 10^5$, $Ma = 0.1$

In Figure 4.7, frame (a) resembles frame (g). So frames (a) through (g) show one period of vortex shedding. The small-scale vortical structures shedding from the leading-edge are in turn captured by the primary vortex and feeding into the rolling-up process of the primary vortex. After leaving the leading-edge, both A- and B-family vortices experience severe deformation as they are stretched and captured by the primary vortex. The flow pattern inside the core of the primary vortex resembles that of the spiral instability mode, which is also observed in the experiment (Rieley & Lowson, 1998). In the numerical simulation, these small-scale vortical structures dissipate quickly as they are leaving the leading-edge and entering the central region of the primary vortex. But in the experiment the spiral instability can evolve into transition. The fast dissipation of the spiral mode in the numerical simulation can be attributed to the insufficiency of resolution. Because grids are clustered near the wall and near the leading-edge of delta wing, in the areas far away from the wall the resolution is relatively low. The future effort will be devoted to increasing the resolution where the primary vortex locates.

Because the small-scale vortical structures are shedding continuously from the leading-edge, the area near the leading-edge is of particular interesting in present work. The detailed pictures of vortex-shedding near the leading-edge is shown in Figure 4.8, where the limiting streamline and contours of axial vorticity of various instance on a cross-section at $x = 0.87L$ are displayed. Through (a) to (h) in Figure 4.8, the pattern of limiting streamline exhibits a periodic feature. Actually, figures (a) to (g) fit in one period of variation. In Figure 4.8(a), there is a secondary vortex attaching on the upper surface of delta wing. The strong leading-edge shear layer is shown by dark color of the contours of axial vorticity. Near the leading-edge, the shear layer is concentrated in a narrow area. In Figure 4.8(b), at $t = 55.68L/U_\infty$, a small vortex shown by the limiting streamline appears near the leading-edge over the free shear layer. In the same picture, a small bulge appears on the shear layer. The generation of this small vortex can be attributed to the Kelvin-Helmholtz instability. Therefore, the small vortex is named as the Kelvin-Helmholtz (K-H) type vortex. At the same time, the secondary vortex, which was attaching on the wing surface at $t = 55.54L/U_\infty$, moves away from the wall. As the K-H type vortex grows, the secondary vortex is pushed further away from the wall. From $t = 55.81L/U_\infty$ to $t = 55.95L/U_\infty$, (Figure 4.8(c) to (d)) the secondary vortex moves upward and begins to separate from the wall, which is corresponding to the B-family vortex, whose rotating direction is opposite to the primary vortex. Therefore, the B-family vortex comes from the shedding of the secondary vortex. The generation of the leading-edge K-H type vortex also causes the deformation of the shear layer, which is visible from the contours of the axial vorticity in Figure 4.8(b), (c), and (d). The bulge on the contours of axial vorticity is corresponding to the K-H type vortex. In Figure 4.8(d), the secondary vortex almost disappears and the K-H type vortex is still attached to the leading-edge. In Figure 4.8(e) and (f), the K-H type vortex grows in size until it reaches the edge of the primary vortex. Another vortex appears at the same location of the secondary vortex, actually it is a new secondary vortex. The K-H type vortex gradually moves upward and sheds from the leading-edge, and comes out to be the A-family vortex, whose rotating direction is the same as the primary vortex. It is obviously that the A-family vortex originates from the K-H type leading-edge vortex. The last two frames are the periodic repeating of frames (a) and (b) in Figure 4.8.

The vortex-shedding near the leading-edge is a periodic process. The interaction between the secondary vortex and the leading-edge shear layer generates a K-H type vortex. As this K-H type vortex grows, the induced flow pushes the secondary vortex away form the wall, and ultimately

leads to the shedding of the B-family vortex. The K-H type vortex grows in size as the secondary vortex shows up again near the wall. The induced flow pushes the K-H type vortex away form the wall and leads to the shedding of the A-family vortex. So the A-family vortex originates from the Kelvin-Helmholtz instability of shear flow near the leading-edge. The B-family vortex originates from the secondary vortex. The period of vortex shedding is between $0.89L/U_\infty$ and $0.98L/U_\infty$. The scale of the K-H type leading-edge vortex and the secondary vortex is about $0.005L$.

The interpretation of the above phenomena is based on the Kelvin-Helmholtz instability of cross-sectional two-dimensional flow. Considering many cross-sections simultaneously, the period of vortex shedding is the same, there is only phase difference between one cross-section and the other. From a three-dimensional point of view, the A- and B-family vortices become vortex tubes, which are oblique to the axial direction.

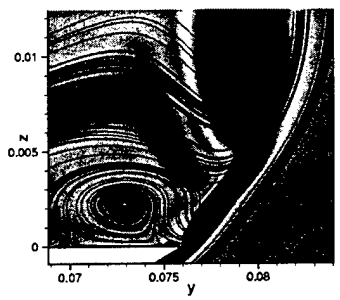

(a) $t = 55.54L/U_\infty$

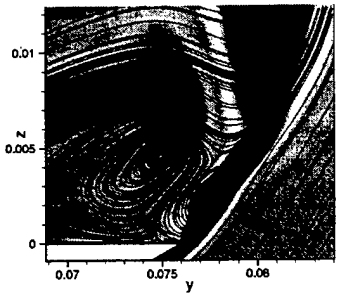

(b) $t = 55.68L/U_\infty$

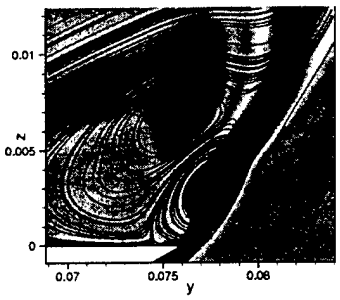

(c) $t = 55.81L/U_\infty$

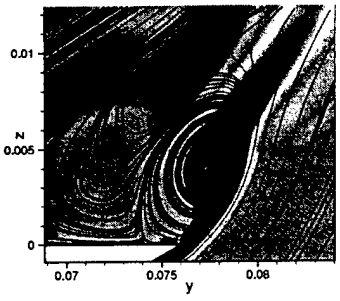

(d) $t = 55.95L/U_\infty$

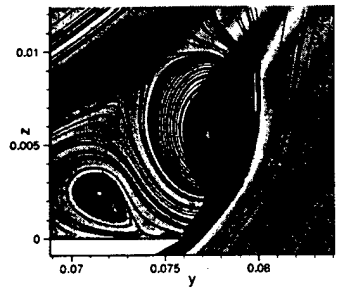

(e) $t = 56.09L/U_\infty$

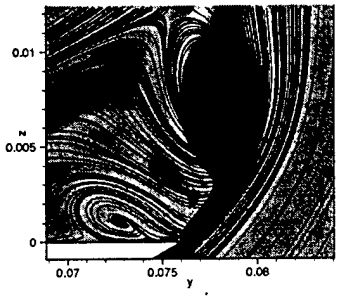

(f) $t = 56.23L/U_\infty$

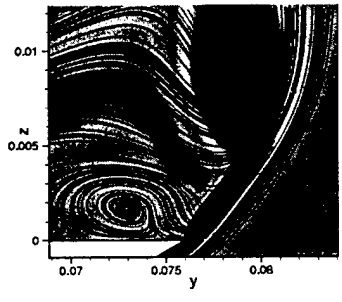

(g) $t = 56.37L/U_\infty$

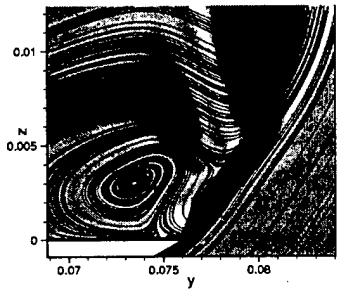

(h) $t = 56.51L/U_\infty$

Figure 4.8: Limiting streamline and contours of axial vorticity of different time on a cross section at $x = 0.87L$. Angle of attack $\alpha = 12.5°$, $Re = 1.96 \times 10^5$, $Ma = 0.1$

The time series of three components of the instantaneous velocity at a location near the leading-edge ($x = 0.87L$, $y = 0.076L$, $z = 0.0094L$) are recorded and shown in Figure 4.9, 4.10, and 4.11. This probe point locates on the cross-section shown in Figure 4.7 and Figure 4.8, so that the velocity signals can be interpreted in accordance with the two-dimensional vortex shedding pictures. The signals of the three components of velocity are all periodic functions of time. The axial velocity u has two local maximums and two local minimums within a period. There are only one local maximum and one local minimum within a period for the signals of the spanwise velocity v and the vertical velocity w. The phase difference between v and w is approximately $\pi/2$, which can be interpreted as a result of the small-scale vortical structure passing through the probe.

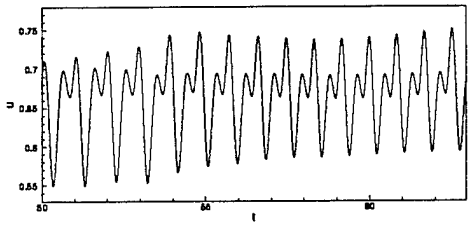

Figure 4.9: Instantaneous axial velocity at a location of $x = 0.87L$, $y = 0.076L$, $z = 0.0094L$

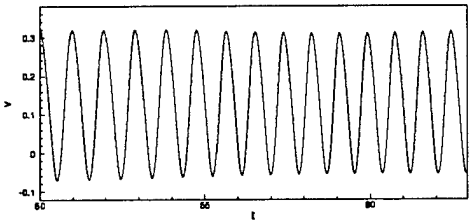

Figure 4.10: Instantaneous spanwise velocity at a location of $x = 0.87L$, $y = 0.076L$, $z = 0.0094L$

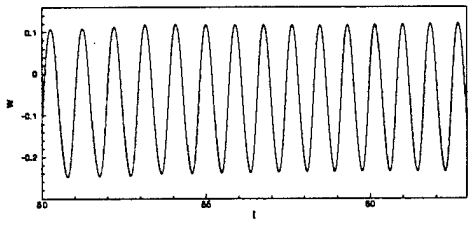

Figure 4.11: Instantaneous vertical velocity at a location of $x = 0.87L$, $y = 0.076L$, $z = 0.0094L$

In order to compare the axial velocity signal with the vortex and shedding pictures in Figure 4.8, a part of Figure 4.9 has been enlarged and shown in Figure 4.12, where those points with the same time as the frames of Figure 4.8 have been marked with the same letter through (a) to (g). In Figure 4.12, one period starts at point (a) and ends at point (g). Compared with Figure 4.8, it has been found that the local minimum at point (d) with a smaller axial velocity value is corresponding to the B-family vortex. As the B-family vortex moves through the probe point, as shown in Figure 4.8(c) and (d), the axial velocity u decreases from point (c) to point (d) and reaches its

local minimum in Figure 4.12. Then the axial velocity recovers as the B-family vortex leaves the probe point. It is followed by the shedding of an A-family vortex from the leading-edge. Before the central part of the A-family vortex reaches the probe point, the axial velocity u signals recorded by the probe increases from point (e) to (f) in Figure 4.12. Then it decreases again from (f) to (g) as the core of the A-family vortex moves through the probe. Therefore, the local minimum at point (g) is associated with the A-family vortex. The local minimum at point (g) has a relatively larger value of axial velocity compared with the local minimum at point (d), which is related to the B-family vortex. The center of both A- and B-family vortices is low-momentum region. Since the B-family vortex originates from the shedding of the secondary vortex near the upper surface of the delta wing, and it brings fluid with lower axial velocity, the central part of the B-family vortex has a lower momentum. The A-family vortex comes from the shedding of leading-edge K-H type vortex. It brings fluid from the free shear layer, which has a relatively larger momentum. In Figure 4.12, the local maximum at point (b) is corresponding to frame (b) of Figure 4.8, where both the A- and B-family vortices have not separated from the delta wing. The signals of the spanwise and the vertical velocity can be interpreted in a similar way. In Figure 4.11, the local maximum is corresponding to the passing of a B-family vortex, where the vertical velocity is positive. The local minimum is corresponding to the passing of an A-family vortex, where the vertical velocity is negative. Thus the period of velocity signals reflects the elapsed time at which the A- and B-family vortices are shedding from the delta wing. Thus the period of vortex-shedding can be measured as the distance between the peaks of local maximums or local minimums on the signals of three velocity components.

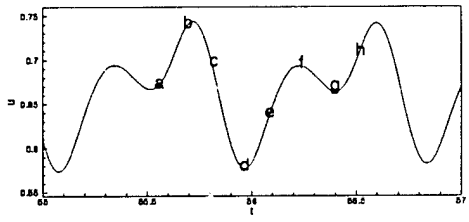

Figure 4.12: Instantaneous axial velocity at location $x = 0.87L$, $y = 0.076L$, $z = 0.0094L$

In order to estimate the vortex-shedding period more accurately, power spectrums of velocity fluctuations are calculated based on the velocity signals and shown in Figure 4.13, 4.14, and 4.15. The velocity fluctuation is calculated as the difference between the instantaneous velocity and the temporal-averaged mean velocity. There are two peaks in the spectrum of the axial velocity fluctuation shown in Figure 4.13. The frequency of the first peak is $1.086U_\infty/L$ and $2.31U_\infty/L$ for the second peak. There is only one peak in the spectrum of the spanwise and vertical velocity fluctuation. The peak frequency is $1.086U_\infty/L$, which is the same as the first peak of the u' spectrum in Figure 4.13. This peak frequency value $f = 1.086U_\infty/L$ represents the frequency of vortex shedding, the corresponding period is $T = 0.9208L/U_\infty$. The higher frequency in Figure 4.13, corresponding to a time period of $T = 0.433L/U_\infty$, reflects the elapsed time between the shedding of a A-family vortex and a B-family vortex, which is approximately half the period of the shedding of a single A- or B-family vortex.

The temporal-averaged velocity profiles distributed on a spanwise line above the upper surface of the delta wing on a cross section at $x = 0.87L$ is shown in Figure 4.16. The distance between

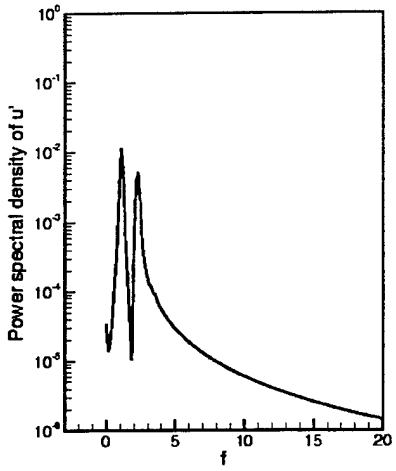

Figure 4.13: Power spectrum density of u' at location $x = 0.87L$, $y = 0.076L$, $z = 0.0094L$

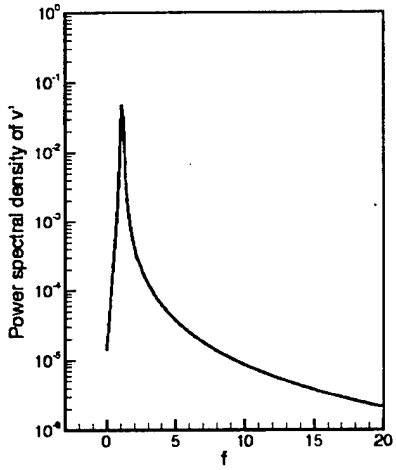

Figure 4.14: Power spectrum density of v' at location $x = 0.87L$, $y = 0.076L$, $z = 0.0094L$

the spanwise line and the wing surface is denoted by the vertical coordinate z in Figure 4.16. These results are in good agreement with the experiments carried out by Rieley & Lowson (1998). As it was stated by Rieley & Lowson (1998), the axial velocity profile indicates the windward boundary layer separation. The inflection point on the axial velocity profile is similar to the Kelvin-Helmholtz instability in plane mixing layers. In Figure 4.16(b), the spanwise velocity profile near the surface (z=0.0002L) changes sign near $y = 0.0746L$, which is corresponding to the re-attachment point of the secondary vortex. The inflection points on profiles of the vertical velocity component in Figure 4.16(c) are corresponding to the edge of the leading-edge shear layer. The inflection point moves outboard as the distance from the wing surface increases. The negative part of the vertical velocity is corresponding to the secondary vortex. The secondary vortex is still visible in the temporal-averaged results. The evidence of vortex shedding has been removed by the temporal average procedure. The point of inflection on the velocity profile is associated

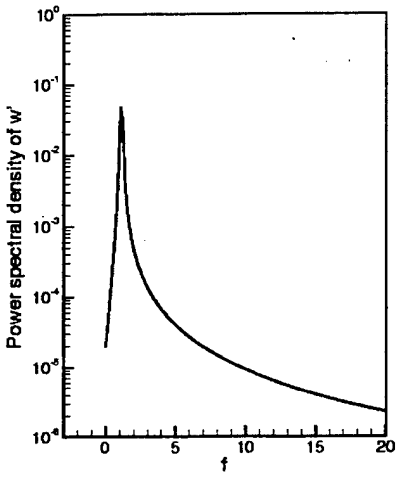

Figure 4.15: Power spectrum density of w' at location $x = 0.87L$, $y = 0.076L$, $z = 0.0094L$

with inviscid instability. Rayleigh's inflection point theorem, studying the instability of a two-dimensional velocity profile based on the linear normal mode approach, points out that disturbance can be amplified at the point of inflection. The physical interpretation of the theorem was given by Lin (1945). The restoring mechanism will force a fluid particle displaced vertically in either direction to return to its starting position. But at the point of inflection the restoring mechanism is not present and disturbance can grow. In the flow around the slender delta wing, the situation is more complex. On the two-dimensional cross section plane, which is vertical to the axial direction, a strong shear layer is observed near the leading-edge, as shown in Figure 4.8(a). The existence of the secondary vortex increases the strength of the shear layer and provides more chance for the generation of the Kelvin-Helmholtz instability.

4.5 Conclusions

Direct numerical simulation has been carried out to simulate the flow around a slender flat-plate delta wing at 12.5° angle of attack. Two Reynolds number have been selected. At a lower Reynolds number of 5×10^4, the flow is stable and dominated by a pair of leading-edge primary vortices. At a higher Reynolds number of 1.96×10^5, small-scale votical structures are shedding from the leading-edge. It has been found that the shedding of the small-scale vortical structures originates not only from the Kelvin-Helmhotz type instability of the leading-edge shear layer, but also from the separation of the secondary vortex form the wing surface. The interaction between the secondary vortex and the Kelvin-Helmholtz type vortex is of particular interesting. The periods of vortex shedding are obtained from the time series of velocity components. The distributions of the temporal-averaged velocity near the upper surface of the delta wing obtained from the computational results agree well with those from the experiment of Rieley & Lowson (1998). But the steady small-scale vortical structures observed in the same experiment have not been found in the current simulation results. However, some unsteady vortical structures were also observed in the experiment, which could be related to the unsteady small vortices found in the computational

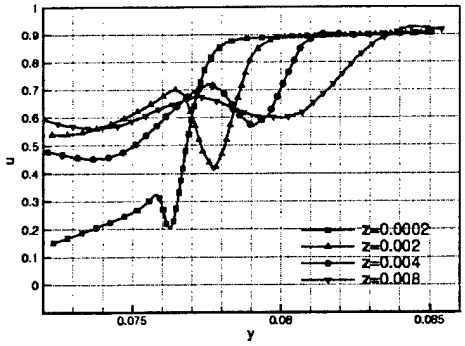

(a) Profiles of average axial velocity

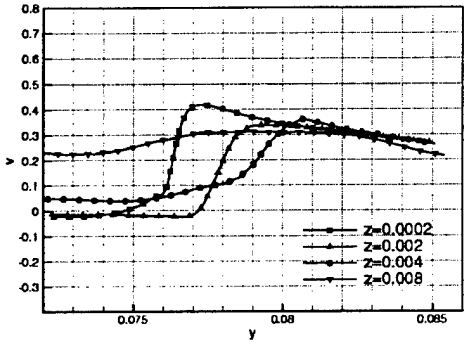

(b) Profiles of average spanwise velocity

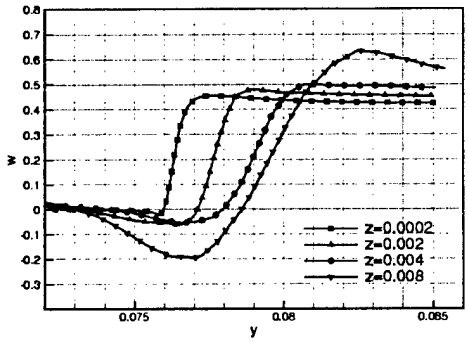

(c) Profiles of average vertical velocity

Figure 4.16: Variations in the three components of temporal-averaged velocity at the leading-edge with increasing distance from the wing surface within on a cross section at $x = 0.87L$

results.

Bibliography

[1] Arena, A. V., and Muellet, T. J. (1980) Laminar separation, transition, and turbulent reattachment near the leading edge of airfoils. *AIAA Journal*, **18**(7), pp.747–753

[2] Agrawal, S., Barnett, R. M., and Robinson, B. A. 1992. Numerical investigation of vortex breakdown on a delta wing. *AIAA Journal*, **30**(3), pp.584–591.

[3] Cipolla, K. M., Liakopoulos, A., and Rockwell, D. O. 1998. Quantitative imaging in proper orthogonal decomposition of flow past a delta wing. *AIAA Journal*, **36**(7), pp.1247–1255.

[4] Cipolla, K. M., and Rockwell, D. 1998. Small-scale vortical structures in crossflow plane of a rolling delta wing. *AIAA Journal*, **36**(12), pp.2276–2278.

[5] Gad-el-Hak, M., and Balckwelder, R. F. 1985. The discrete vortices from a delta wing. *AIAA Journal*, **23**(6), pp.961–962.

[6] Gordnier, R. E., and Visbal, M. R. 1994. Unsteady vortex structure over delta wing. *Journal of Aircraft*, **31**(1), pp.243–248.

[7] Jiang, L., Shar, H, Liu, C., Visbal, M. R., 1999. Non-reflecting boundary condition in curvilinear coordinates. *Second AFOSR International Conference on DNS/LES*, Rutgers, New Jersey, June 7-9.

[8] LeLe, S. K. 1992. Compact finite difference schemes with spectral-like resolution. *J. Comput. Phys.* **103**, pp.16-42.

[9] Modiano, D. L., and Murman, E. M. 1994. Adative computations of flow around a delta wing with vortex breakdown. *AIAA Journal*, **32**(7), pp.1545–1547.

[10] Riley, A. J., and Lowson, M. V. 1998. Development of a three-dimensional free shear layer. *J. Fluid Mech.*, **369**, pp.49–89.

[11] Payne, F. M., Ng, T. T., Nelson, R. C., and Shiff, L. B. 1988. Visualization and wake surveys of vortical flow over a delta wing. *AIAA Journal*, **26**(2), pp.137–143.

[12] Shih, C., Lourenco, L., Van Dommelen, L., and Krothapalli, A. (1992) Unsteady flow past an airfoil pitching at a constant rate. *AIAA Journal*, **30**(5), pp.1153–1161

[13] Shih, C., Lourenco, and Krothapalli, A. (1995) Investigation of flow at leading and trailing edge of pitching-up airfoil. *AIAA Journal*, **30**(5), pp.1369–1376

[14] Spekreijse, S.P. (1995) Elliptic grid generation based on Laplace equations and algebraic transformation. *J. Comp. Phys.*, **118**, pp.38–61

[15] Tenaud, C., and Phuoc, L. T. (1997) Large eddy simulation of unsteady, compressible, separated flow around NACA 0012 airfoil. *Lecture Notes in Physics.* **490**, pp.424–429.

[16] Thompson, J. F., Warsi, Z. U. A., and Mastin, C. W. (1985) *Numerical Grid Generation: Foundations and Applications.* Elsevier, New York

[17] Van Dommelen, L. and Shen (1980) The Spontaneous generation of singularity in a separating laminar boundary layer. *J. of Compt. Phys.*, **38**, pp.125–140.

[18] Van Dommelen, L. and Cowley, S. J. (1990) On the Lagrangian description of unsteady boundary layer, Part 1: General theory. *J. Fluid Mech.*, **210**, pp.593–626.

[19] Visbal, M. R., and Gordnier, R. E. 1995. Origin of computed unsteadiness in the shear layer of a delta wing. *Journal of Aircraft*, **32**(5), pp.1146–1148.

[20] Visbal, M. R. 1995. Computational and physical aspects of vortex breaksown on delta wings. *AIAA Paper* 94-2317

[21] Visser, K. D., and Nelson, R. C. 1993. Measurements of circulation and vorticity in the leading-edge vortex of a delta wing. *AIAA Journal*, **31**(1), pp.104–111.

[22] Wu, J-Z., Lu, X., Denny, A. G., Fan, M., and Wu, J-M. (1999) Post-stall flow control on an airfoil by local unsteady forcing. *J. Fluid Mech.*, **371**, pp.21–58.

[23] Yoon, S., Kwak D. 1992. Implicit Navier-Stokes solver for three-dimensional compressible flows, *AIAA Journal* **30**, pp.2653-2659